

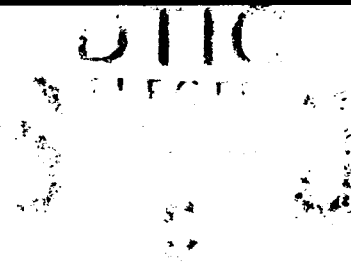
AD-A243 285



2

TECHNICAL REPORT BRL-TR-3302

**BRL**



REAL-TIME LOCATION OF  
IMPACT ON A PLANAR SURFACE

THOMAS KOTTKE  
GEORGE M. THOMSON

DECEMBER 1991

APPROVED FOR PUBLIC RELEASE; DISTRIBUTION IS UNLIMITED.

U.S. ARMY LABORATORY COMMAND

BALLISTIC RESEARCH LABORATORY  
ABERDEEN PROVING GROUND, MARYLAND

91-17607



91 1211 022

## **NOTICES**

**Destroy this report when it is no longer needed. DO NOT return it to the originator.**

**Additional copies of this report may be obtained from the National Technical Information Service, U.S. Department of Commerce, 5285 Port Royal Road, Springfield, VA 22161.**

**The findings of this report are not to be construed as an official Department of the Army position, unless so designated by other authorized documents.**

**The use of trade names or manufacturers' names in this report does not constitute indorsement of any commercial product.**

**UNCLASSIFIED**

<b>REPORT DOCUMENTATION PAGE</b>			<b>Form Approved</b> <b>OMB No. 0704-0188</b>	
<small>Public reporting burden for this collection of information is estimated to average 1 hour per response, including the time for reviewing instructions, searching existing data sources, gathering and maintaining the data needed, and completing and reviewing the collection of information. Send comments regarding this burden estimate or any other aspect of this collection of information, including suggestions for reducing this burden, to Washington Headquarters Services, Directorate for Information Operations and Reports, 1215 Jefferson Davis Highway, Suite 1204, Arlington, VA 22202-4302, and to the Office of Management and Budget, Paperwork Reduction Project (0704-0188), Washington, DC 20503.</small>				
<b>1. AGENCY USE ONLY (Leave blank)</b>		<b>2. REPORT DATE</b> December 1991	<b>3. REPORT TYPE AND DATES COVERED</b> Final, 1 April 1990-1 July 1991	
<b>4. TITLE AND SUBTITLE</b> Real-Time Location of Impact on a Planar Surface			<b>5. FUNDING NUMBERS</b>  PE: 61221A	
<b>6. AUTHOR(S)</b>  Thomas Kottke and George M. Thomson				
<b>7. PERFORMING ORGANIZATION NAME(S) AND ADDRESS(ES)</b>			<b>8. PERFORMING ORGANIZATION REPORT NUMBER</b>	
<b>9. SPONSORING / MONITORING AGENCY NAME(S) AND ADDRESS(ES)</b>  U.S. Army Ballistic Research Laboratory ATTN: SLCBR-DD-T Aberdeen Proving Ground, MD 21005-5066			<b>10. SPONSORING / MONITORING AGENCY REPORT NUMBER</b>  BRL-TR-3302	
<b>11. SUPPLEMENTARY NOTES</b>				
<b>12a. DISTRIBUTION / AVAILABILITY STATEMENT</b>  Approved for public release; distribution is unlimited.			<b>12b. DISTRIBUTION CODE</b>	
<b>13. ABSTRACT (Maximum 200 words)</b>  A proof-of-principle integrated hardware-software system has been developed which rapidly measures impact locations on a planar surface. This device operates by measuring the rate of charge transfer along an electrically resistive sheet from the point of impact to a series of charge collection tabs. Both one-dimensional and two-dimensional transducer geometries have been investigated. A collection of calibration and correction software routines has been developed to increase impact location accuracy. The performance of this system has been evaluated for both laboratory and simulated field conditions. Multihit capability has been investigated by evaluating system performance with damaged transducer surfaces. Schematic diagrams are included of all electronic circuitry as well as listings of all software routines.				
<b>14. SUBJECT TERMS</b>  impact location; position (location); impact sensor; position sensor; impact point			<b>15. NUMBER OF PAGES</b> 60	
			<b>16. PRICE CODE</b>	
<b>17. SECURITY CLASSIFICATION OF REPORT</b> UNCLASSIFIED	<b>18. SECURITY CLASSIFICATION OF THIS PAGE</b> UNCLASSIFIED	<b>19. SECURITY CLASSIFICATION OF ABSTRACT</b> UNCLASSIFIED	<b>20. LIMITATION OF ABSTRACT</b> SAR	

**UNCLASSIFIED**

INTENTIONALLY LEFT BLANK.

# TABLE OF CONTENTS

	<u>Page</u>
LIST OF FIGURES .....	v
LIST OF TABLES .....	vi
ACKNOWLEDGMENTS .....	vii
1. INTRODUCTION .....	1
2. EXPERIMENTAL PROCEDURE .....	2
2.1 System Hardware .....	2
2.1.1 Position Sensing Transducer .....	2
2.1.2 Signal Processing .....	4
2.2 System Software .....	5
2.2.1 Software Overview .....	5
2.2.2 Calibration Software .....	6
2.2.3 Data Acquisition, Correction, and Display Routine .....	11
2.3 System Test and Evaluation .....	11
2.3.1 Hardware Testing .....	11
2.3.2 Software Evaluation .....	15
2.3.3 Simulated Field Testing .....	23
2.4 One-Dimensional Measurements .....	30
2.4.1 Position Sensing Transducer .....	30
2.4.2 One-Dimensional Preliminary Results .....	30
3. SUMMARY .....	32
4. REFERENCES .....	37
APPENDIX A: SIGNAL PROCESSING CIRCUITRY .....	39
APPENDIX B: POSITION DETECTOR SYSTEM SOFTWARE .....	47
DISTRIBUTION LIST .....	59

Acquisition File  
 Date: \_\_\_\_\_  
 DTIC File # \_\_\_\_\_  
 Government Use \_\_\_\_\_  
 Justification \_\_\_\_\_  
 By \_\_\_\_\_  
 Distribution \_\_\_\_\_  
 Classify by \_\_\_\_\_  
 Date \_\_\_\_\_  
 A-1

**INTENTIONALLY LEFT BLANK.**

## LIST OF FIGURES

<u>Figure</u>	<u>Page</u>
1. Geometry of Position Sensor Active Surface .....	3
2. Block Diagram of Position Sensor Signal Processing Unit .....	5
3. Schematic Overview of Software Units .....	7
4. Ideal Position Sensor X Axis Output Characteristics .....	7
5. Uncorrected Position Sensor X Axis Output Characteristics .....	8
6. Ideal Position Sensor X and Y Output Characteristics .....	9
7. Uncorrected Position Sensor X and Y Output Characteristics .....	9
8. Output From Charge Amplifiers (Right) as a Function of Charge Deposition Position (Left) .....	13
9. Nonmaskable Interrupt Signal Delay Time .....	14
10. Analog Division Circuit Output Settling Time .....	14
11. Corrected Position Sensor X Axis Output Characteristics .....	16
12. Corrected Position Sensor X and Y Output Characteristics .....	16
13. Residual Values for Uncorrected X Axis Position Measurements With Three- Dimensional Representation at the Top and Two-Dimensional Representation at the Bottom .....	17
14. Residual Values for X Axis Software-Corrected Position Measurements With Three-Dimensional Representation at the Top and Two-Dimensional Representation at the Bottom .....	17
15. Histogram of Raw X Values .....	21
16. Magnitude of the X Axis Span Which Contains 90% of the Software-Corrected Positions With Three-Dimensional Representation at the Top and Two- Dimensional Representation at the Bottom .....	22
17. Regions of the Active Surface Which Contain 90% of the Software-Corrected Position Measurements of a 17 by 17 Test Grid .....	22
18. Position Error vs. Confidence Level .....	24

<u>Figure</u>		<u>Page</u>
19.	Position Error vs. Confidence Level for Simulated Field Test Data .....	29
20.	Corrected Position Sensor X and Y Output Characteristics for a Damaged Active Surface .....	29
21.	Geometry of One-Dimensional Position Sensor Active Surface .....	31
22.	Uncorrected One-Dimensional Position Sensor Output Characteristics .....	31
23.	Corrected One-Dimensional Position Sensor Output Characteristics .....	32
A-1.	Schematic of Dual Channel Charge Amplifiers .....	42
A-2.	Schematic of Sample and Hold Circuitry .....	42
A-3.	Schematic of Analog Division Circuitry .....	44
A-4.	Schematic of Differential Voltage Amplifier .....	45

#### LIST OF TABLES

<u>Table</u>		<u>Page</u>
1.	Dependence of Confidence Level on Position Error .....	24
2.	Dependence of Position Measurement on Charge Storage Capacitor Magnitude .....	25
3.	Position Sensor Simulated Field Test Data .....	27
4.	Position Sensor Error Parameters .....	34



## **ACKNOWLEDGMENTS**

The authors gratefully acknowledge the contributions of Dr. Charles Hummer of the Engineering Physics Branch, U.S. Army Ballistic Research Laboratory (BRL), who graciously spent many hours discussing electronic details and unraveling coaxial rats' nests. The authors would also like to thank Dr. Jerry Thomas and members of the Probability and Statistics Branch, BRL, for helpful discussions concerning statistical analysis. The authors would like to thank Earl N. Ferry, Jr., of the Launch and Flight Division, BRL, for his assistance with illustration scanning. And finally, the authors would like to thank BRL's David C. Hackbarth and Dr. Clint Hollandsworth for reviewing and improving the manuscript.

INTENTIONALLY LEFT BLANK.

## 1. INTRODUCTION

The ability to sense a penetration event and determine the point of impact on a two-dimensional surface is a necessary prerequisite for many existing and future armor systems. The degree of sophistication of these measurements covers a wide range and is mandated by the testing or systems requirements. For some studies, such as evaluation of aiming and projectile accuracy, a "post-event" determination of impact point is sufficient. This type of analysis can be as rudimentary as finding where the holes are in a target. The time of the penetration event needs to be accurately and rapidly determined if the dynamics of the projectile-armor interaction are to be investigated by flash x-ray, high-speed optical cameras, or other analysis equipment. For high resolution analysis, the location of the penetration event may also need to be determined.

The break-wire screen has been the standard tool for sensing penetration events and measuring their location in real-time. A typical embodiment of this apparatus includes a series of parallel, isolated electrical conductors arranged in a plane which is normal to the path of the projectile. For a two-dimensional determination of location, a second array is included where the conductors are perpendicular with respect to the conductors in the first array. As a projectile passes through this grid, it breaks some of the conductors, causing a loss of electrical contact. The time of the initial penetration event can be denoted by feeding all the signals from the individual conductors into an AND gate and sensing the change of state of the output. A subsequent poll of the states of the individual conductors reveals the location of the penetration event.

Advantages of the break-wire method include the overall simplicity of the concept, its immunity to noise, and its intrinsically digital nature. However, in spite of the simplicity of the concept, the standard application of this technique can present substantial engineering difficulties. The requirement of numerous isolated conductors and separate circuitry for each wire, or multiplexers, to monitor the state of the screen can make the task of installing and maintaining such a system tedious or even impractical. To ensure that a projectile will break at least one conductor, the spacing between adjacent conductors can not exceed the projectile diameter. Therefore, complexity grows rapidly when the impact site of small objects must be established over a large area.

The present study seeks development of an alternative method for measuring impact sites on a two-dimensional surface. A proof-of-principle device resulted which can easily be scaled up to monitor large surfaces and has the ability to determine positions before the impacting ballistic projectile can travel a significant distance. The solution offered here rests upon creating a charge flow from the impact point through an electrically resistive medium to the extremities of the sensing surface. A measurement of the relative rate of flow to each sensor edge indicates the impact location. In principle, this type of sensing surface can be expanded to any reasonable size without changing the nature of its operation. The determination of the impact location in the proof-of-principle device takes a few tens of microseconds, a figure which can doubtless be reduced substantially. Finally, the device is inexpensive, simple, and can be fabricated from readily available materials and components.

## 2. EXPERIMENTAL PROCEDURE

### 2.1 System Hardware.

2.1.1 Position Sensing Transducer. The active surface of the position sensor consists of an electrically resistive square sheet with four charge collection tabs fixed along the outer edges. The geometry of the active surface and collection tabs is illustrated in Figure 1. When electrical charge arrives on this surface, it raises the local potential, causing the charge to flow outward to the collection tabs. The resistance of the sheet is set so that the rate at which charge is collected by the four tabs depends on their distance to the point where the charge is initially deposited. The closer a tab is to the point of charge deposition, the lower the effective path resistance to the tab and the higher the rate of charge transfer and collection. By comparing the relative amounts of charge collected by the tabs on opposing sides of the sensing surface (e.g.,  $X_1$  vs.  $X_2$  and  $Y_1$  vs.  $Y_2$ ), the position of the point of charge deposition along each axis can be deduced.

The resistive sheet material is prepared by impregnating vellum paper with fine grain graphite particles. This recipe arose from tests of several fabrication schemes, mostly involving various means of spraying and soaking of graphite in a volatile solvent. The simple rubbing of the graphite powder into the paper surface is the easiest and yields the most uniform sheet resistivities. Although beyond the scope of this report, it may be possible to

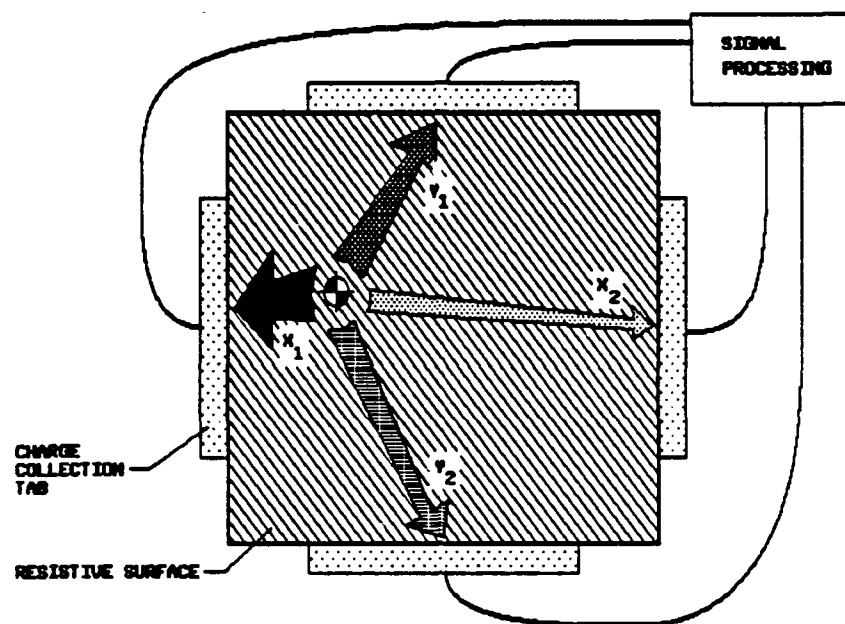


Figure 1. Geometry of Position Sensor Active Surface.

optimize the performance of the position sensor by adjusting the sheet resistivity of the impregnated particulate material by the addition of conducting/insulating materials to the graphite base and by adjusting the distribution of resistivity on the active surface. All of the experimental results presented in this report were obtained using a 20-cm by 20-cm sensing surface. The collection tabs consisted of 10-cm-long blocks which were covered with copper-foil tape and mechanically connected to the edges of the resistive sheet to yield an insignificant electrical contact resistance. The nominal resistance on the sensing surface was 150 ohms between opposing tabs and 125 ohms between normal tabs.

There are a variety of potential methods for depositing charge to the position sensor's active surface. For field applications, a small capacitor can be connected to a thin metallic sheet which closely covers, but does not actually touch, the active surface. When impacted by an object, the metallic sheet deforms and deposits the charge from the capacitor at the point of impact. With an appropriate increase in surface resistivity, piezoelectric plastic films might be utilized in a similar manner with the added advantage of making the discharge capacitor unnecessary.

For laboratory testing and calibration, it is important to repeatedly deposit charge on the active surface at known locations. To facilitate such testing, a metallic cover plate which had an array of small holes spanning the entire active surface of the position detector was used. By passing a fine metallic probe through these holes, the cover plate could be shorted to the active surface and the charge deposited at a well defined location. The charge was stored in a 220-pF capacitor charged to -15 V. A 5,100-ohm resistor was connected between the capacitor and cover plate to regulate the discharge current. The charge collection tabs were coupled through 0.1- $\mu$ F capacitors to the signal processing electronics. This AC coupling offered a high resistance to 60-cycle noise. A large resistor was also connected between the active surface and ground to prevent the undesirable buildup of deposited charge.

**2.1.2 Signal Processing.** A significant feature of the position sensor's signal processing unit is the relative insensitivity to the actual amount of charge which is deposited to the active surface. This broad range of acceptable charge deposition is achieved by measuring the rates at which charge is collected rather than the total amount of charge. An added benefit of this approach is the enhanced speed made possible by a measurement strategy which operates while the charge is being transferred rather than having to wait until all the charge has been collected. An overview of the signal processing unit is illustrated in the block diagram of Figure 2. Detailed schematics and descriptions of all electronic circuitry are in Appendix A.

The first step in measuring the rate of charge transfer is to convert the charge collected at the four tabs into amplified voltage signals. This task is performed by the charge amplifiers. When the sum of the voltage signals for each pair of opposing tabs reaches a predetermined threshold level, the individual voltage signals and their sum are captured by sample and hold circuits. An analog division circuit then determines the value of the quotient  $\frac{\text{tab 2 signal}}{\text{tab 1 signal} + \text{tab 2 signal}}$ . This representation for combining the signals from opposing tabs provides results that are a linear function of the charge collected at each tab between the well defined limits of 0 and 1. The seemingly simpler representation  $\frac{\text{tab 1 signal}}{\text{tab 2 signal}}$  yields a distinctly nonlinear result between the ill-defined limits of 0 and  $\infty$ . A voltage amplifier which can vary the DC offset as well as the amplitude of the quotient signal is used. This allows the output signal to be set at a convenient level for viewing by oscilloscope or

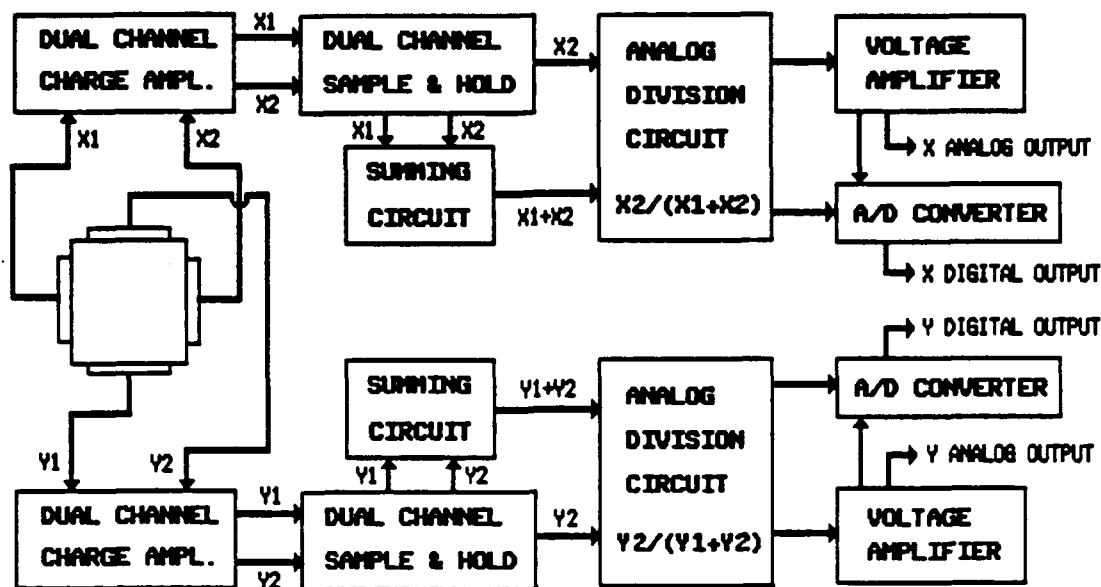


Figure 2. Block Diagram of Position Sensor Signal Processing Unit.

other analog display instrumentation. In addition, the voltage amplifier expands the range of possible analog output signals to completely cover the measurement range of subsequent analog to digital converters in order to achieve maximum conversion resolution. These digitized signals are readily accessible for computer-controlled calibration and display.

## 2.2 System Software.

**2.2.1 Software Overview.** In order for this position sensor to be integrated into a decision-making or control environment, its output signals should be converted to digital form. Analog to digital (A/D) conversion of the voltage amplifier output signals (Figure 2) is performed with the assistance of computer control. The use of computer control requires associated software drivers. For system software development, an Apple IIe (Apple Computer Inc., Cupertino, CA) computer is used as the controller with high level programs written in Applesoft BASIC and machine language routines written for the 6502 microprocessor. The 1-MHz clock frequency and interpreted high level language do not yield a particularly fast system by today's standards. However, this setup is more than adequate for determining system feasibility and

developing software logic. Digital conversions are performed by an 8-bit ADC0816 (National Semiconductor Corporation, Santa Clara, CA) monolithic analog-to-digital converter controlled by the microprocessor.

The software that controls the data acquisition system can be divided into the overlapping categories of system calibration, data acquisition, data correction, and data display. A schematic illustrating the interaction between the software units that perform these tasks is shown in Figure 3. High level language code is denoted by boxes with rounded corners while data files are shown as rectangles. Machine code that is accessed by a high level language routine is indicated by a dashed box.

**2.2.2 Calibration Software.** An added advantage of computer control is the potential for sophisticated system calibration and data correction. The ideal output characteristics for one dimension of a two-dimensional position sensor are illustrated in Figure 4. In this example, the determined X position is plotted as a function of the actual X and Y positions,  $X_a$  and  $Y_a$ . For the ideal case, the determined X position is linearly proportional to  $X_a$  and is not a function of  $Y_a$ . The other dimension would have similar characteristics. That is, the determined Y position would be independent of  $X_a$  and linearly proportional to  $Y_a$ .

Figure 5 illustrates the actual raw output characteristics for the position sensor in the X direction. In order to realize maximum resolution and accuracy, the zero offset and scale of the voltage amplifiers is first adjusted so that the raw X values,  $X_r$ , cover roughly the entire range of allowed values. The data are then obtained by measuring  $X_r$  values for each element in the grid of known actual positions ( $X_a, Y_a$ ) across the active surface of the position sensor. In contrast to the ideal characteristics shown in Figure 4, the actual output characteristics are neither independent of  $Y_a$  nor particularly linear with respect to  $X_a$ . Therefore, any data correction scheme must treat a corrected value for the X position,  $X_c$ , to be a function of both the raw X and Y data values:

$$X_c = f(X_r, Y_r). \quad (1)$$



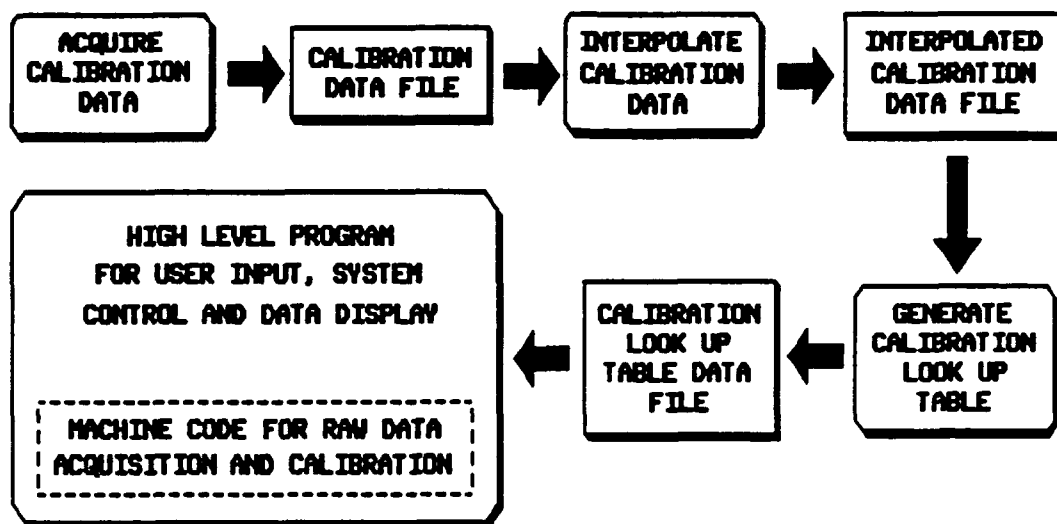


Figure 3. Schematic Overview of Software Units.

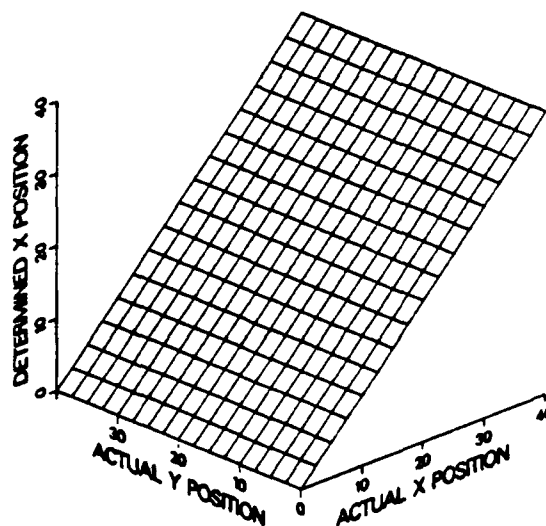


Figure 4. Ideal Position Sensor X Axis Output Characteristics.

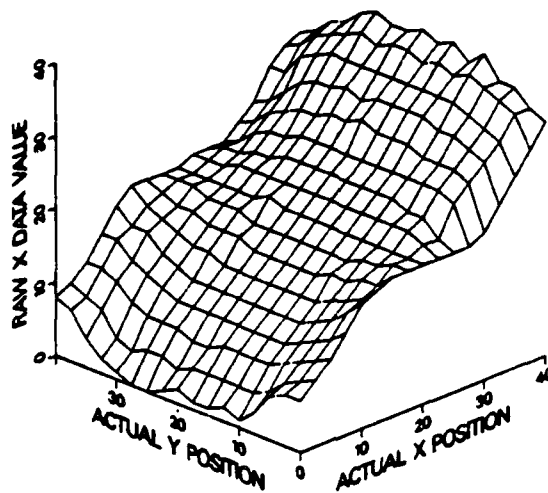


Figure 5. Uncorrect Position Sensor X Axis Output Characteristics.

Similarly, for the corrected value of the Y position,  $Y_c$ :

$$Y_c = g(X_r, Y_r). \quad (2)$$

At minimum and maximum values for  $Y_a$ , the raw  $X_r$  values for centrally located actual positions,  $X_a$ , are pinned to a median value by the presence of the two charge collection tabs which are simultaneously measuring the Y position. Thus, instead of defining an inclined ramp in position space, the position sensor's raw output characteristics define a curved saddle-like shape which clearly illustrates the need for data correction processing.

The plots in Figures 4 and 5 consider the output characteristics of only a single dimension of the two-dimensional position sensor. In order to simultaneously represent the transducer response of both axes, the plots of Figures 6 and 7 are convenient. Figure 6 illustrates the output characteristics from an idealized two-dimensional position sensor. The determined positions from a regular array of actual positions ( $X_a, Y_a$ ) generate a linear grid. By contrast, Figure 7 shows that only the centrally located positions of the position sensor yield an approximately regular grid of raw data values. A major source of this distortion is the

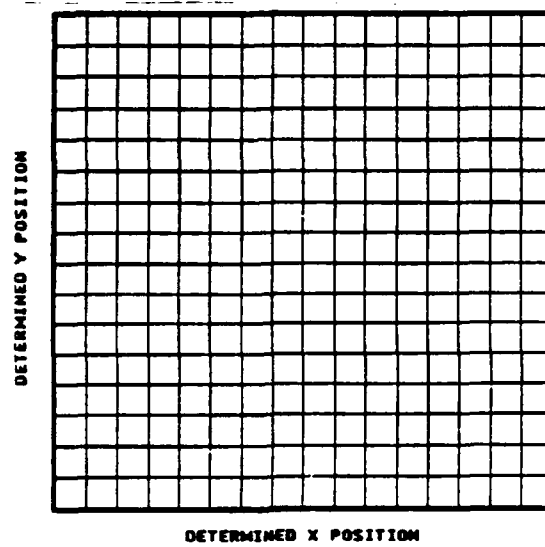


Figure 6. Ideal Position Sensor X and Y Output Characteristics.

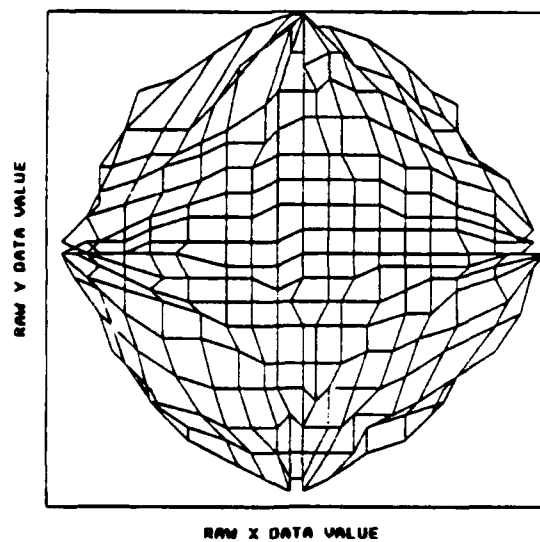


Figure 7. Uncorrected Position Sensor X and Y Output Characteristics.

presence of the charge collection tabs. When charge is deposited in a corner position, the charge collection tabs on the adjacent edges offer a low resistance path to the other side of the active surface. The apparent point of deposition is therefore located at a more central position. One obvious remedy for this problem would be to reduce the length of the charge collection tabs. However, the use of overly short tabs can lead to an increased number of positions which yield nonunique raw data values. Future efforts devoted to refining this position detector should include studies to determine the optimal charge collection tab geometries. At any rate, once again the need for data correction processing is clear.

A first step in calibrating the position sensor is to obtain raw calibration data by depositing charge at a matrix of known locations on the sensor surface. This calibration data is of the type shown in Figure 5. Each value of raw position output from the sensor is normalized and rounded off to integral values from 0 to 39. In this representation, the smallest increment of position corresponds to 1/40th of full scale. This scaling is performed to match the low resolution graphics capability of the Apple IIe, which will eventually also serve as the display device.

To measure the response of the position detector at all 1,600 locations on a 40 by 40 grid would be excessively tedious. Therefore, data are acquired on a more manageable 17 by 17 grid which is stored in a data file. Maximum resolution for the corrected position value ultimately to come from this device ( $X_c, Y_c$ ) still requires one to know the raw data ( $X_r, Y_r$ ) on a full 40 by 40 grid of points. Thus, the data file for the 17 by 17 array of experimentally measured raw data is run through another high level routine which interpolates the data to a 40 by 40 array of points and stores this information in an additional file. The errors introduced by the interpolation procedure are insignificant.

The array is then inverted, and a look-up table of corrected positions associated with each possible raw data pair is stored in a calibration data file—a file which is indexed by its raw data values. The look-up table, which in operation is stored in computer memory, is intended to form a bridge between the raw and corrected data sets. When the device responds to an impact by recording a raw data position ( $X_r, Y_r$ ), a high level routine scans the memory for the address indexed by this pair and reports the corresponding corrected position ( $X_c, Y_c$ ) stored therein.

The goal of this effort and indeed the measure of this device's worth is that the corrected position should be equal to the actual position,  $(X_a, Y_a)$ . The high level routines which interpolate the calibration raw data matrix and generate the look-up table are listed in Appendices B-1 and B-2.

**2.2.3 Data Acquisition, Correction, and Display Routine.** An additional high level routine, one dedicated to controlling actual impact data acquisition, is listed in Appendix B-3 along with a detailed accounting of the associated memory configuration. This routine acquires raw data, uses the calibration look-up table to correct the data, and then displays the result. To increase the speed of the data acquisition process, this high level routine calls a machine language routine to control the A/D chip for the actual data acquisition. The assembler listing of this machine code routine is also listed in Appendix B-4.

After the machine language A/D driver is called and the raw data is scaled and corrected, the corrected position is graphically indicated on the computer monitor by the intersection of two cross hairs. With the output signal from the position sensor available in both analog and digital form, a wide range of display, control, and decision-making procedures could now be implemented.

## **2.3 System Test and Evaluation.**

**2.3.1 Hardware Testing.** When charge is deposited to the resistive active surface of the position sensor, it immediately begins to flow to the array of tabs along the edges. The rate at which charge is collected at each tab depends on the electrical resistance, or distance, between the deposition point and the tab in question. Once collected, the charge is processed by a charge amplifier (Figure A-1), the output waveform of which is dependent on the position of charge deposition. Figure 8 shows the output from two charge amplifiers connected to opposing tabs along one dimension of the position sensor for a series of charge deposition locations. An illustration of the relative positions of the tabs and charge deposition point is shown on the left with the associated oscillogram of the charge amplifier outputs on the right. For clarity, the baselines of the two oscilloscope traces have been offset. The scales for all the oscillograms are as noted in the upper figure. The oscilloscope is

pretriggered to allow the baseline levels to be recorded. In each case, the actual time of triggering is at or near the first indication of activity above the base level.

When charge is deposited on the left portion of the sheet, the distance to the *A* tab is much less than the distance to the *B* tab, causing the effective resistance to the *A* tab to also be less. Thus, the rate of charge collection at the *A* tab should be greater than at the *B* tab, an inference corroborated by the greater slope of trace *A* in the associated oscillogram. As the charge deposition point is moved to the right, the rate of charge collection at tab *A* decreases while the charge collection rate at tab *B* increases. When charge is deposited in the middle of the sheet, the collection rate at the two tabs is approximately equal as indicated by the equal slopes of the two charge amplifier output signals. As the point of charge deposition is moved farther to the right, the trend continues with greater charge collection rates and amplifier signal slopes being noted for tab *B*.

The output from the charge amplifiers is routed to the sample and hold circuitry shown schematically in Figure A-2. In the first stage of this circuit, the sum of the signals from the charge amplifiers is compared against a preset voltage threshold level to determine when the signals are to be latched. After the threshold level has been exceeded, it is important that the delay time of the triggering signal to the sample and hold elements be small so that the outputs from the charge amplifiers will not saturate before being latched. Figure 9 shows an oscillogram of the response time of the nonmaskable interrupt (NMI) signal. The lower trace shows the voltage waveform as measured directly at a charge collection tab which denotes the time of charge deposition. The upper trace shows the subsequent drop of the NMI line. The submicrosecond response time of the NMI line is well within the available time window for sampling the outputs from the charge amplifiers as illustrated in Figure 8.

Another important response time is the amount of time between the deposition of the charge and the settling of the analog division circuitry (Figure A-3). This is, in fact, a measurement of the total time required to make an analog measurement of the charge deposition position. Figure 10 shows the output from the analog division circuit where the voltage waveform from a collection tab is again used to denote the time of charge deposition. The total time required from deposition until the quotient achieves an asymptotic value is approximately 25  $\mu$ s. Inasmuch as the circuitry used here was constructed from

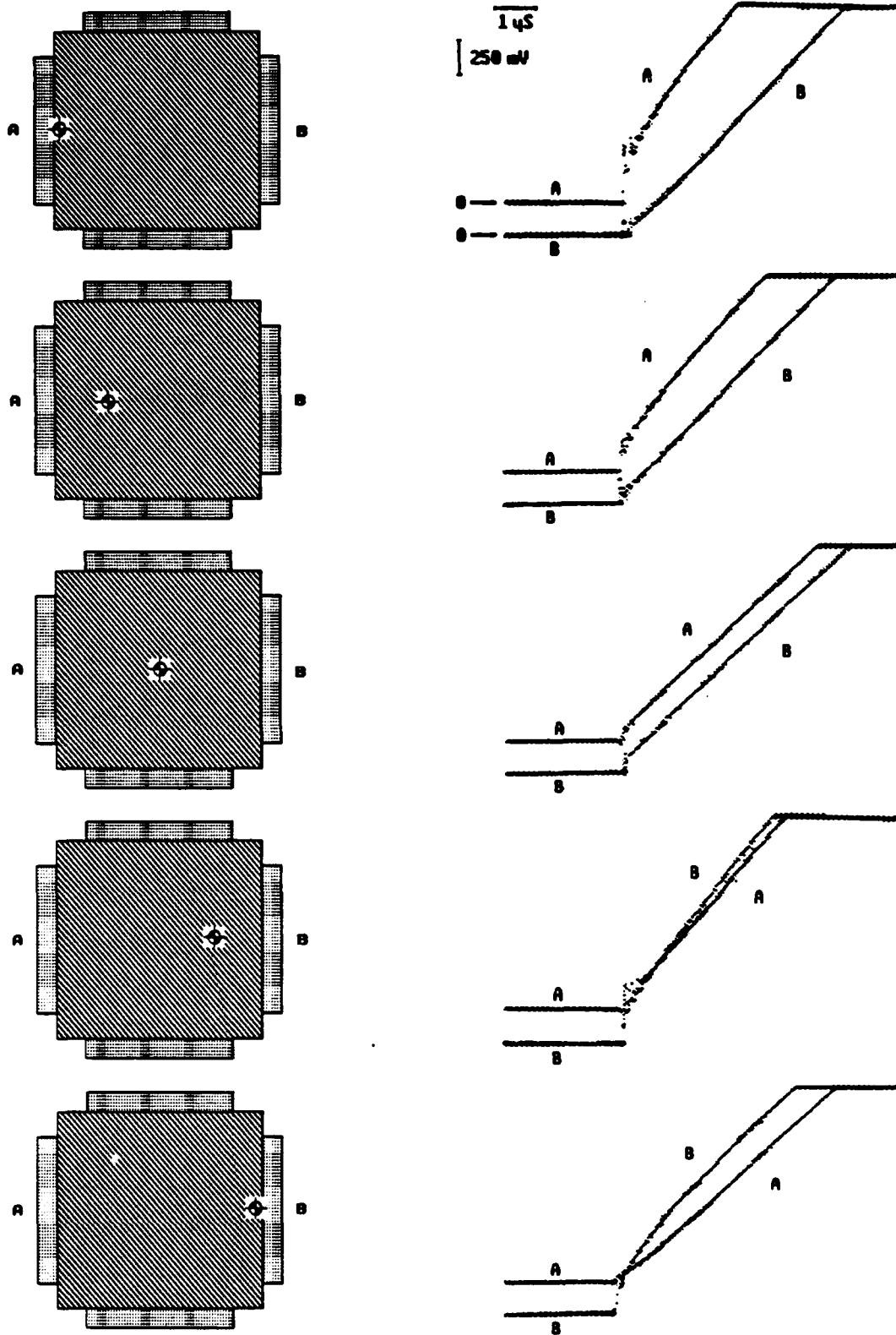


Figure 8. Output From Charge Amplifiers (Right) as a Function of Charge Deposition Position (Left).

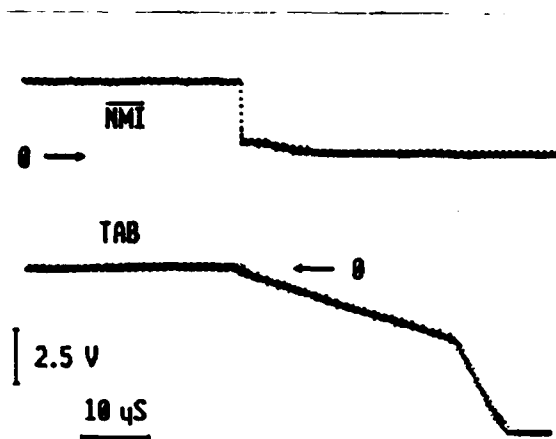


Figure 9. Nonmaskable Interrupt Signal Delay Time.

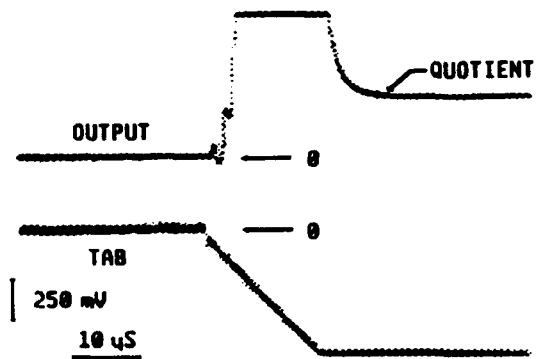


Figure 10. Analog Division Circuit Output Settling Time.



generic components which are not specifically designed for short-cycle times, substantial reduction in measurement times should be possible. The use of commercially available divider modules should halve the recorded measurement time.

**2.3.2 Software Evaluation.** As illustrated in Figures 4 and 5, the uncorrected position sensor output does not accurately reproduce the desirable characteristics associated with an idealized position sensor. That is, the uncorrected output from the position sensor is neither a highly linear function of the actual position along the axis of determination, nor is it independent of the actual position along the orthogonal axis. It is for these reasons that the previously described correction software is utilized. In order to test the effectiveness of the correction software, a set of data is taken for which 20 position measurements are recorded at each location of a 17 by 17 grid spanning the active surface. Figure 11 shows the mean data value at each position when the software correction is implemented. The corrected output from the position sensor shows that the majority of the saddle-like distortion associated with the uncorrected response of Figure 5 has been eliminated. Note that deviations from the idealized inclined plane output characteristics are predominantly localized to the perimeter of the active surface.

Figure 12 simultaneously illustrates the corrected response from both axes of the position sensor. Comparison with the uncorrected response, of Figure 7 shows that the data correction software has significantly improved the correlation between the measured and ideal response as illustrated in Figure 6.

In order to quantitatively discuss the amount of distortion associated with the uncorrected and corrected position sensor response, it is convenient to consider the residual values associated with each case. In this context, the residual value is defined to be the difference between the actual location of charge deposition and the mean location as determined by the position sensor. A residual value of zero therefore indicates an exact determination of position with the magnitude of nonzero residuals reflecting the amount of error, or lack of accuracy, associated with the measurement.

Figure 13 illustrates the residuals associated with the uncorrected position sensor data in two different formats. On the top, a three-dimensional plot of residuals graphically displays

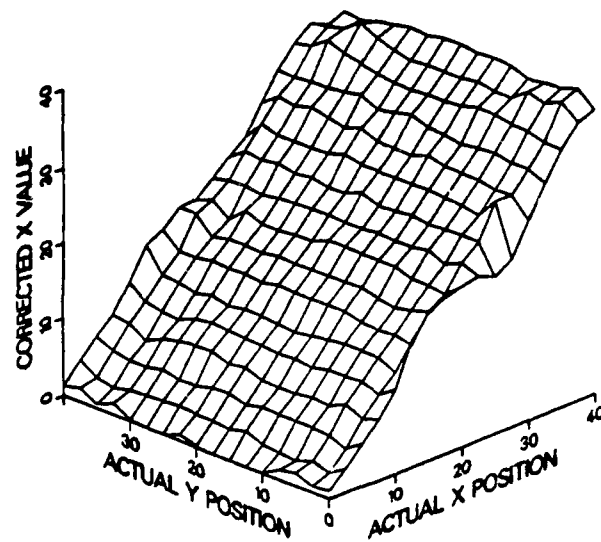


Figure 11. Corrected Position Sensor X Axis Output Characteristics.

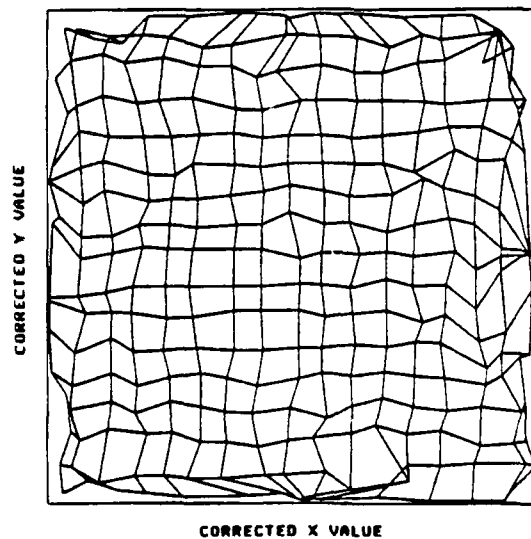


Figure 12. Corrected Position Sensor X and Y Output Characteristics.

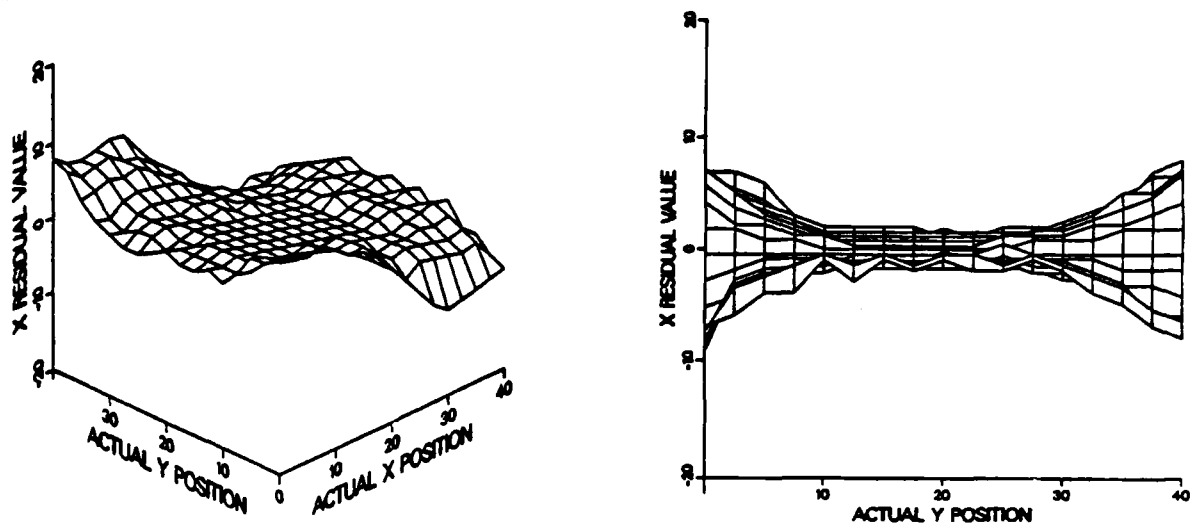


Figure 13. Residual Values for Uncorrected X Axis Position Measurements With Three-Dimensional Representation at the Top and Two-Dimensional Representation at the Bottom.

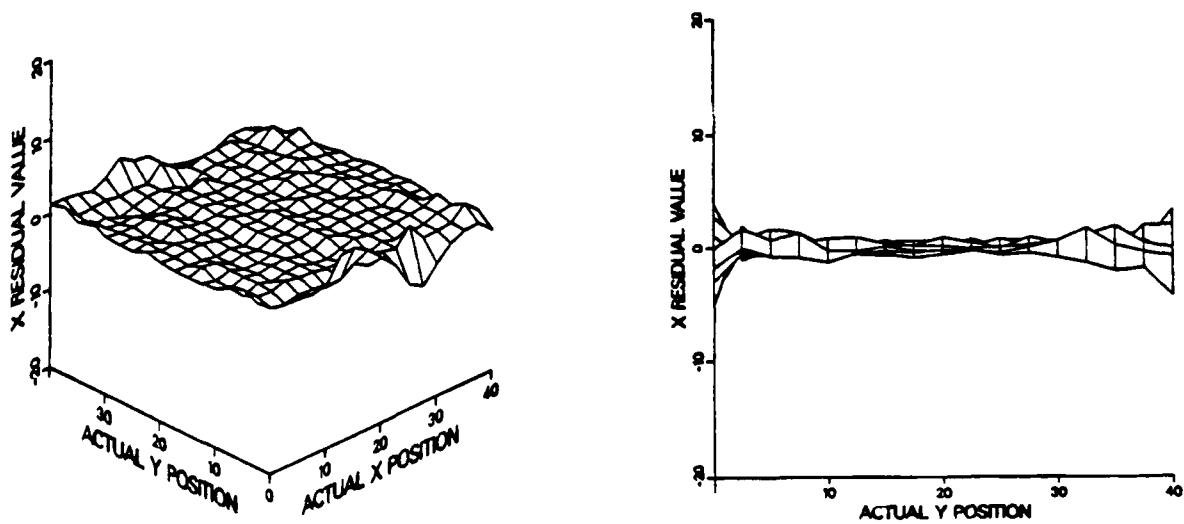


Figure 14. Residual Values For X Axis Software-Corrected Position Measurements With Three-Dimensional Representation at the Top and Two-Dimensional Representation at the Bottom.

the relative magnitude and sense of the errors associated with each measurement location. This type of plot is useful for conveying an overall image of where the accuracy of the system is limited. In this type of representation, an idealized position sensor has a three-dimensional residual plot which is a plane with an X residual value of zero. For a more quantitative assessment, a two-dimensional plot of the same data is more useful, as shown on the lower figure. In this illustration, the actual X position axis has been compressed by plotting the X residual value vs. the actual Y position for the family of actual X positions. The figure on the bottom can also be thought of as the figure on the top when viewed from a vantage point located a large distance down the actual X position axis. The envelope defined by this family of curves represents the "worst-case" errors associated with the uncorrected X position measurements,  $X_u$ , at each actual Y position. This two-dimensional plot clearly shows that the greatest errors in the uncorrected X position measurement occur for minimum and maximum values of the actual Y position. As previously discussed, the enhanced error along the edges of the active surface is due to the presence of the charge collection tabs used for simultaneous measurements of the position in the orthogonal direction. The worst-case error for the uncorrected X axis data is located in this region with a magnitude of 9.2 parts out of 40 or 23% of full scale. Combining the X and Y axis data, the worst-case error for the uncorrected  $X_u, Y_u$  data is 12.0 parts out of 40 or 30% of full scale.

The effective accuracy of the position sensor can be improved by limiting the functional region of the active surface to an interior area. This accuracy increase is obviously associated with a decrease in position sensing coverage. If the working active surface is taken to be the area defined by the inner 15 by 15 grid of data points, instead of the entire 17 by 17 grid of the active surface, the usable sensing area is reduced to 76%. In this interior region, the worst-case error for the uncorrected X axis data drops to 6.7 parts out of 40 or 17% of full scale. The worst-case error for the combined  $X_u, Y_u$  data is reduced to 7.9 parts out of 40 or 20% of full scale.

The two-dimensional plot of Figure 13 highlights the worst-case data points but offers little quantitative information about the average error associated with the position measurements. Numerical analysis of the full area sensor data yields an average residual magnitude for the uncorrected X axis data of 2.5 parts out of 40 or 6.3% of full scale. For the combined  $X_u, Y_u$  data, the average residual magnitude is 4.0 parts out of 40 or 10% of full scale. The average

residual magnitude for the X axis data in the previously defined interior region drops to 2.0 parts out of 40 or 5% of full scale. In this same region, the average residual magnitude of the combined  $X_c, Y_c$  data is 3.2 parts out of 40 or 8% of full scale.

Similar plots of the residual values for software-corrected measurements are shown in Figure 14. The three-dimensional plot on the top can be seen to more closely approximate the planar residual plot of an idealized position sensor. On the bottom, the reduced envelope of the two-dimensional plot shows that the worst-case accuracy errors have been significantly reduced. For the full area sensor, the worst-case error for the corrected X axis data is 5.1 parts out of 40 or 13% of full scale. The average residual magnitude for the X axis data over this full area is 0.55 parts out of 40 or 1.4% of full scale. The combined  $X_c, Y_c$  data shows a worst-case error of 7.1 parts out of 40 or 18% of full scale and an average residual magnitude of 0.9 parts out of 40 or 2.3% of full scale. Once again, the most significant accuracy errors are localized along the perimeter of the active surface. Therefore, the effective accuracy of the position sensor can again be increased at the expense of usable sensing area. For the previously defined interior area, the worst-case error for the corrected X axis data drops to 2.0 parts out of 40 or 5% of full scale while the average residual magnitude is reduced to 0.36 parts out of 40 or 0.9% of full scale. In this same region, the combined  $X_c, Y_c$  data worst-case error drops to 3.6 parts out of 40 or 9% of full scale while the average residual magnitude is reduced to 0.63 parts out of 40 or 1.6%.

The utility of the software correction process in reducing accuracy errors is revealed by comparing the errors for the uncorrected and corrected cases. For the full area sensor, the correction routines reduce the absolute worst-case error for the X axis data from 23% to 13% and the average residual magnitude from 6.3% to 1.4%. Over the full area of the sensor, the correction routines reduce the combined X and Y data worst-case error from 30% to 18% and the average residual magnitude from 10% to 2.3%. If only the interior 76% of the active surface area is utilized, the software correction drops the X axis data worst-case error from 17% to 5% while the average residual magnitude decreases from 5% to 0.9%. The effect of the software correction on the combined X and Y axis data in the interior region is to reduce the worst-case error from 20% to 9% and the average residual magnitude from 8% to 1.6%. Thus, the correction routines decrease the worst-case error by approximately a factor of two and the average residual magnitudes by a factor of four or five.

The previous discussion and quantitative analysis of the calibration of the position sensor utilizes calibration and test data comprised of the mean values of an ensemble of measurements at each tested location. Therefore, these determined accuracies are an indication of the average error between the actual and measured positions. In addition to the accuracy associated with position measurements, it is also important to consider the precision, or reproducibility, of these measurements. This precision measurement describes the range of values over which the ensemble of measurements is spread. Figure 15 qualitatively displays the reproducibility of five sets of X value data. These data were collected by recording 500 sequential raw X values at 5 different locations on the position sensor's active surface. The data in sets A, B, C, D, and E correspond to actual X positions of 7, 14, 21, 28, and 34. A centrally located actual Y position was used for all of these tests. In general, the distributions for these measurements are not symmetrical. This is particularly true for measurements taken near an edge of the active surface. Therefore, these data are not normally distributed, and a simple standard deviation should not be used to represent the range of data values. Instead, the precision is quantified by ranking the individual measurements and specifying the range of values over which a given percentage of the data is contained. For these test data, the range of values which contains 90% of the individual measurements will be considered. Since 20 data values were recorded at each location, this is equivalent to removing the lowest and highest values and determining the span in position of the 18 centrally ranked measurements.

The magnitudes of the spans of X axis values which contain 90% of the software-corrected measurements are illustrated graphically in Figure 16. The formats of the plots and the magnitudes of the axes scales are similar to previous plots to facilitate direct comparison. Once again, the largest errors are localized along the outer edges of the active surface. The largest recorded span in X values which contained 90% of the individual measurements over the full area sensor was 12 parts out of 40 or 30% of full scale. However, the average X value span for the full area sensor was much lower at 1.74 parts out of 40 or 4.4% of full scale. Over the previously defined interior area, the largest X value span was 8 parts out of 40 or 20% of full scale with an average value of 1.44 parts out of 40 or 3.6% of full scale.

The combined deviations of the individual position measurements along the X and Y axes are illustrated in Figure 17. For each position of the 17 by 17 grid of test locations, the area

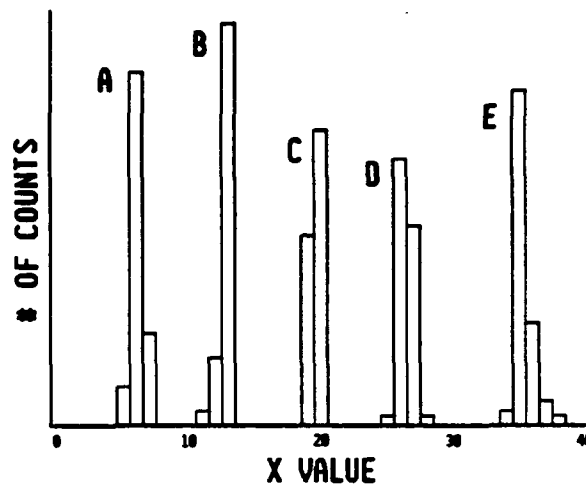


Figure 15. Histogram of Raw X Values.

of the position sensor which contained 90% of the individual measurements is outlined. Small rectangles indicate a close grouping of individual data points while larger rectangles mark areas of greater deviation. Once again, this illustration highlights the fact that the largest deviations are located along the edges of the transducer surface.

Depending on the sense of a deviation with respect to the sense of the associated residual, a deviation from the mean position can either move a recorded position closer to, or farther away from, the actual location. To consider the worst-case situation, it is assumed that the sense of the deviation is the same as the sense of the residual so that these two sources of error will add. Thus, a conservative measure of the overall performance that can be expected from the position sensor is to consider the distance between the actual charge deposition location and the most distant corner of the associated deviation rectangle, as displayed in Figure 17. This distance is termed the "position error." Using this distance to define the radius of a circle, at least 90% of all individual position measurements can be expected to fall within this circle when it is centered at the actual charge deposition location.

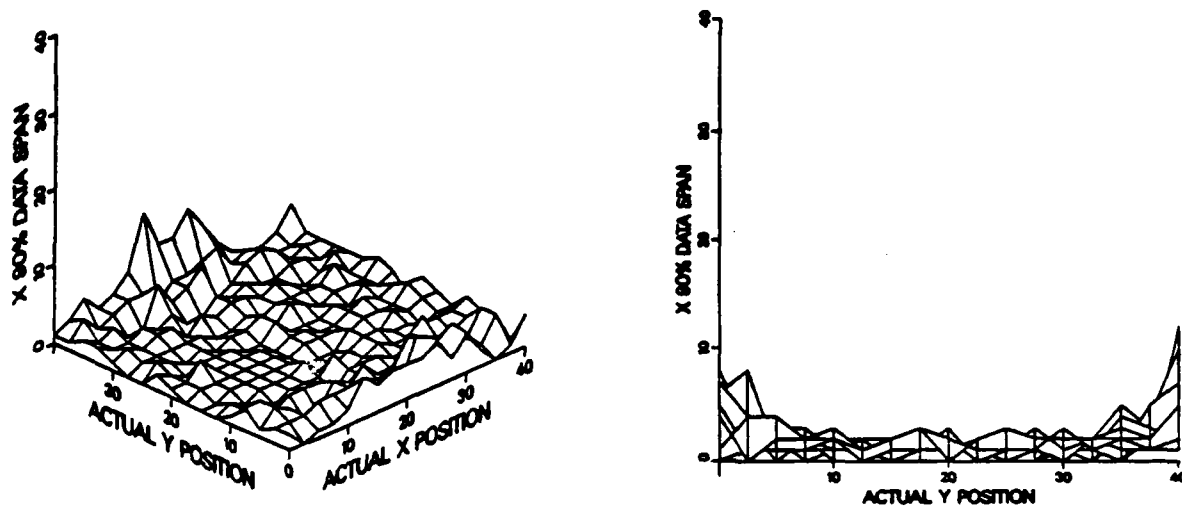


Figure 16. Magnitude of the X Axis Span Which Contains 90% of the Software-Corrected Positions With Three-Dimensional Representation at the Top and Two-Dimensional Representation at the Bottom.

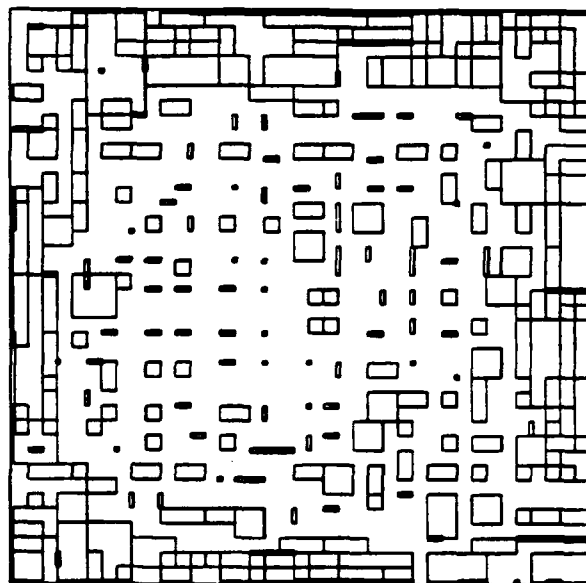


Figure 17. Regions of the Active Surface Which Contain 90% of the Software-Corrected Position Measurements of a 17 by 17 Test Grid.



Figure 18 plots the confidence level that 90% of all randomly located individual position measurements will be within a given position error of the actual charge deposition location. Data are presented for both the full and reduced sensing areas. This plot was constructed from the ranked position errors of the 289 positions of the 17 by 17 grid of test locations. The ranks were normalized from 0% to 100% to form the abscissa while the ranked position errors formed the ordinate. For example, the largest observed position error for the reduced area sensor was 14.5% of full scale. Therefore, the confidence level is 100% that randomly located position measurements will yield individual position measurements such that 90% will be within 14.5% of full scale of the actual position. Similarly, the confidence level is 80% that randomly located position measurements in the reduced area will have 90% of the individual measurements within 6.3% of full scale of the actual position. Selected confidence levels and the associated position errors are tabulated in Table 1.

**2.3.3 Simulated Field Testing.** For laboratory calibration and performance evaluation, a metallic cover plate was used which had an array of small holes spanning the active surface of the position sensor. Charge could be repeatedly deposited at well-defined locations by passing a fine metallic probe through these holes and shorting the cover plate to the active surface. For field applications, the stored charge would be deposited in a somewhat more violent and less controlled manner. The impacting object would deform the cover plate at the point of impact where the stored charge would be transferred to the active surface. These two charge deposition methods are expected to be equivalent because, as previously stated, it is the ratio of charges collected at the various tabs which is critical and not the magnitude of the deposited charge. To test the sensitivity of position determination to the actual amount of deposited charge, a series of measurements was taken using charge storage capacitors of different magnitudes. Position measurements were recorded at five different locations while the charge storage capacitance was varied over six orders of magnitude. Twenty individual position measurements were logged at each position and capacitance value. The X and Y mean positions, 5% rank positions, and 95% rank positions are listed in Table 2 for the various capacitance values. As expected, neither the accuracy nor the reproducibility of the position measurements appear to be affected by the variation in the magnitude of the deposited charge.

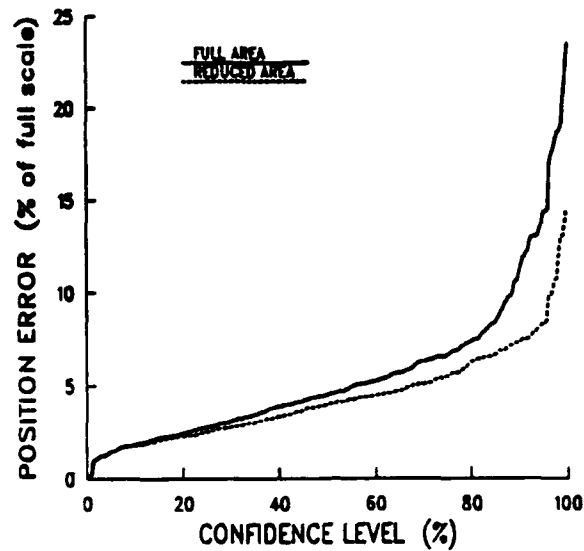


Figure 18. Position Error vs. Confidence Level.

Table 1. Dependence of Confidence Level on Position Error

Confidence Level (%)	Full Error Position Level (% of FS)	Reduced Area Position Error (% of FS)
10	1.9	1.8
20	2.5	2.3
30	3.1	2.8
40	3.9	3.4
50	4.5	4.0
60	5.3	4.5
70	6.3	5.1
80	7.4	6.3
90	11.2	7.3
100	23.5	14.5

Of course the best way to evaluate the field performance of the position detector is to fire projectiles at it. This allows the system to be tested when charge is transferred to the active surface following the deformation of the cover plate. Projectiles of 4.5-mm diameter were

Table 2. Dependence of Position Measurement on Charge Storage Capacitor Magnitude

Location No.	Capacity ( $\mu\text{F}$ )	X Mean Position	X 5% Rank Position	X 95% Rank Position	Y Mean Position	Y 5% Rank Position	Y 95% Rank Position
1	0.0022	21.8	21	22	19.8	19	20
1	0.022	21.8	21	22	19.9	19	20
1	0.22	21.8	21	22	20.0	20	20
1	2.2	21.8	21	22	19.2	19	20
1	22	21.8	21	22	19.1	19	20
1	220	22.2	22	23	19.0	18	20
2	0.0022	13.4	12	14	15.9	15	16
2	0.022	13.6	13	14	16.0	16	16
2	0.22	13.8	13	14	16.0	16	16
2	2.2	13.5	13	14	16.0	16	16
2	22	13.8	13	14	16.0	16	16
2	220	14.0	13	14	16.0	16	16
3	0.0022	18.0	16	19	33.0	32	34
3	0.022	18.6	16	19	32.8	32	34
3	0.22	18.2	16	19	33.2	32	34
3	2.2	18.3	16	19	32.8	32	34
3	22	18.7	16	21	32.8	32	34
3	220	19.2	16	22	33.4	32	34
4	0.0022	27.0	27	28	8.6	8	10
4	0.022	27.1	27	27	8.8	8	10
4	0.22	27.2	27	28	8.7	8	10
4	2.2	27.2	27	28	9.2	8	10
4	22	26.9	26	27	9.8	9	10
4	220	27.8	27	29	9.0	8	10
5	0.0022	32.8	32	33	31.0	31	31
5	0.022	32.8	32	33	31.0	30	31
5	0.22	32.8	32	33	30.7	30	31
5	2.2	32.8	32	33	30.8	30	31
5	22	32.6	32	33	30.4	30	31
5	220	32.6	32	33	30.2	30	31

impacted on the position sensor with a nominal velocity of 100 m/s. The force of these impacts was sufficient to deform and pierce the cover plate with the associated deposition of stored charge. Table 3 lists the recorded analog signal measurement times; raw, corrected, and actual X and Y positions, and position errors. The impact sites were spread over the position sensor active surface in a roughly homogenous pattern. Shots with impact locations outside of the previously defined interior region are denoted by an asterisk next to the test number. Ten of the 37 test shots, or 27%, fell outside this interior region. Since the external region comprises 24% of the active surface, this simulated field test represents a survey of the entire active surface. Figure 19 compares the full area confidence level statistics as determined in the laboratory against the field test results. The laboratory full area position errors include only 90% of the individual position measurements whereas the single-shot statistics of the field tests effectively represent 100% of each shot. In spite of the more stringent definition for the field test position error, the confidence level for a given position error is higher for the field test data than the laboratory simulation. Also, the overall shapes of these two curves are quite similar. This confirms the previous assertion that the performance statistics developed in the laboratory are a conservative estimate of the position sensors capabilities. Thus, the performance of the position sensor as measured in the laboratory is a valid estimate of the field performance of this device.

Another important performance parameter for an impact position sensor is the "multiple-hit" capability. That is, how is the performance of the sensor degraded by the damage sustained during previous impacts? For the previously described field testing, a thick hard back plate was located directly behind the electrically resistive surface. Thus, although the resistive surface was damaged by each test, the active surface was not actually pierced. To study the effect of active surface deterioration on position sensing, a hole was cut into the active surface, and the laboratory performance evaluation was repeated. A 12-mm-diameter hole was cut into the resistive surface which yields a hole size that is 6% of the active surface edge length. This hole was positioned so that it did not coincide with any of the positions of the 17 by 17 grid of test sites. Figure 20 illustrates the relative positions of the test sites and the 12-mm hole. Superimposed on this figure are the corresponding corrected positions. Comparison of Figure 20 with the corrected positions for the undamaged sensor, shown in Figure 12, reveals that the position sensor output characteristics have changed very little. Quantitative analysis confirms this observation. The introduction of the hole in the active surface increases the full area average residual magnitude from 2.3% to 2.6% while the

Table 3. Position Sensor Simulated Field Test Data

Shot No.	Measurement Time (μS)	Raw X	Raw Y	Corrected X	Corrected Y	Actual X	Actual Y	Position Error (%)
1	25	20	7	21	6	19.5	5.8	3.8
2	25	32	20	33	21	33.5	23.8	7.1
3	24	20	34	22	36	20.1	35.0	5.4
4	8	10	19	9	20	6.7	19.8	5.8
5	9	11	13	10	12	9.4	11.7	1.7
6	22	27	15	21	13	28.8	11.6	3.5
7	13	25	26	21	28	28.3	29.3	4.6
8	17	13	27	12	29	10.1	30.2	5.6
9	10	9	8	4	3	1.8	1.8	6.3
10	13	34	12	37	5	38.1	4.6	2.9
11	15	31	30	38	38	38.1	37.6	1.0
12	23	10	30	6	33	2.4	37.8	15.0
13	10	18	19	19	20	17.4	19.5	4.2
14	17	29	18	30	17	29.9	18.3	3.3
15	13	5	22	3	28	3.0	28.6	1.5
16	23	16	6	14	5	12.2	4.0	5.1
17	23	37	17	39	9	36.3	12.5	11.1
18	15	23	34	28	36	30.5	38.1	8.2
19	19	20	27	21	29	19.5	30.3	5.0
20	14	21	18	22	17	22.5	17.5	1.8
21	17	28	11	30	6	30.5	5.8	1.3
22	18	34	25	38	32	37.8	32.3	0.9
23	16	17	32	15	34	12.2	35.3	7.7
24	4	9	13	8	11	6.7	11.0	3.3
25	25	23	24	25	26	24.5	26.2	1.3
26	14	18	13	19	12	17.4	11.9	4.0
27	13	20	4	21	3	20.9	1.5	3.8
28	24	8	18	7	19	5.5	18.4	4.0
29	14	37	19	39	20	37.8	20.0	3.0

Table 3. Position Sensor Simulated Field Test Data (Continued)

Table 3. Position Sensor Simulated Field Test Data (Continued)

Shot No.	Measurement Time (μS)	Raw X	Raw Y	Corrected X	Corrected Y	Actual X	Actual Y	Position Error (%)
30	15	20	35	22	37	25.6	39.0	10.3
31	17	16	22	16	23	14.6	24.4	4.9
32	10	6	12	4	8	3.5	8.2	1.3
33	13	24	3	32	0	32.3	0.9	2.4
34	15	12	31	8	34	6.1	35.3	5.8
35	16	28	30	31	32	32.4	33.5	5.1
36	26	24	12	26	9	25.1	8.5	2.6
37	13	5	18	4	18	1.2	17.4	7.2

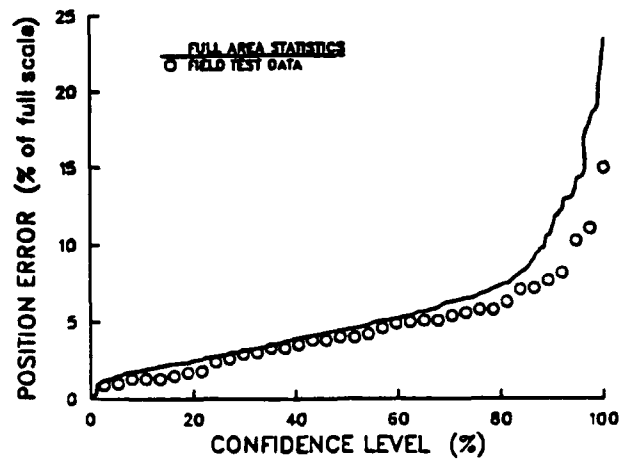


Figure 19. Position Error vs. Confidence Level for Simulated Field Test Data.

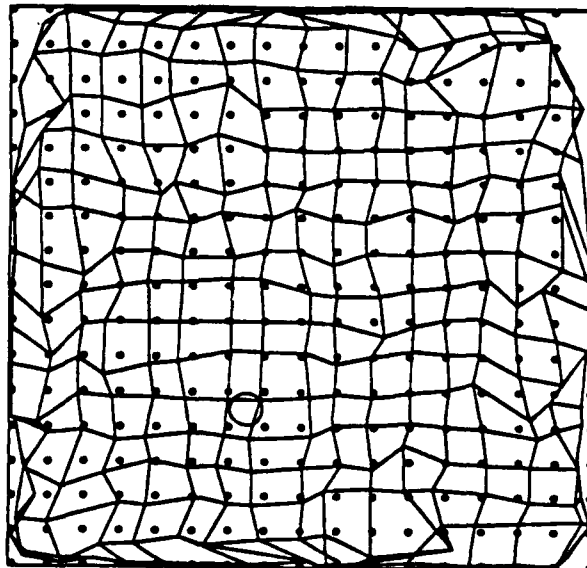


Figure 20. Corrected Position Sensor X and Y Output Characteristics for a Damaged Active Surface.

reduced area average residual magnitude changes from 1.6% to 2.3%. These small increases in average residual magnitude indicate that this impact position sensor exhibits potential for substantial multihit capabilities.

## **2.4 One-Dimensional Measurements.**

**2.4.1 Position Sensing Transducer.** One source of the nonlinearity in the raw response of this impact sensor transducer, and the subsequent need for data correction, is the presence of the charge collection tabs which are simultaneously measuring the position in the orthogonal direction. A logical extension of the results already presented is to consider the performance of the impact sensor with only a single pair of charge collection tabs, as illustrated in Figure 21. For this configuration, the remaining two charge collection tabs are extended to span the entire edge of the active surface to reduce edge effects and more closely approximate an infinitely long one-dimensional system. Of course, this type of arrangement can only provide position information along the axis which is normal to the collection tabs. However, a second transducer surface with the collection tabs oriented in the orthogonal direction could be used to provide impact information along the second dimension for a complete two-dimensional position determination. The added complication of the second transducer surface may be more than offset by the potential for projectile velocity measurements. By measuring the time interval between the impacts of the projectile on the two transducers, and knowing the separation distance between the transducers, the projectile velocity can be determined.

**2.4.2 One-Dimensional Preliminary Results.** Figure 22 illustrates the raw output characteristics for the one-dimensional position sensor. In contrast to the raw output characteristics of the transducer surface, which simultaneously measured positions in two dimensions (shown in Figure 5), the one-dimensional transducer response is quite linear. The raw output from the one-dimensional transducer does not completely span the range of determined values. One method for correcting this deficiency is to employ the previously described software correction techniques. The one-dimensional corrected output characteristics are illustrated in Figure 23. However, the true worth of the one-dimensional measurement scheme may lie in the potential for completely eliminating the need for computer-controlled data correction. By modifying the output stage electronics to expand the



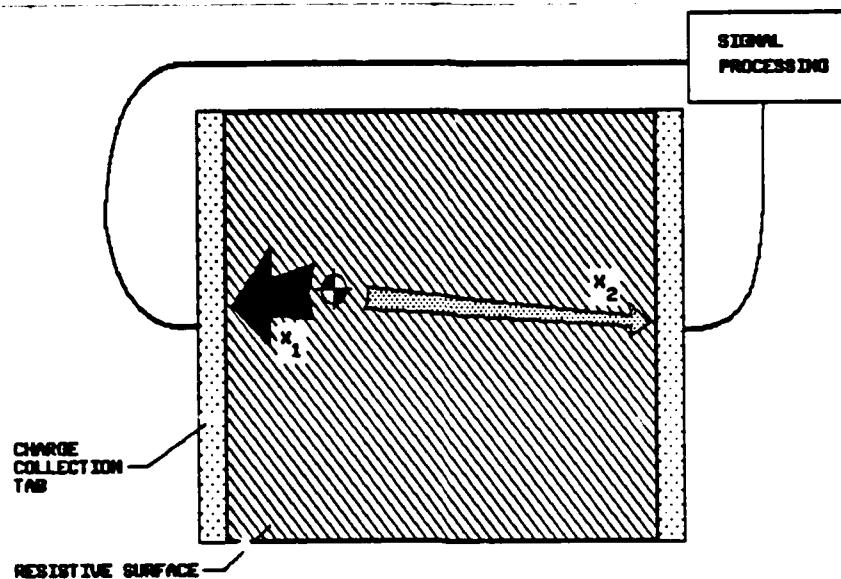


Figure 21. Geometry of One-Dimensional Position Sensor Active Surface.

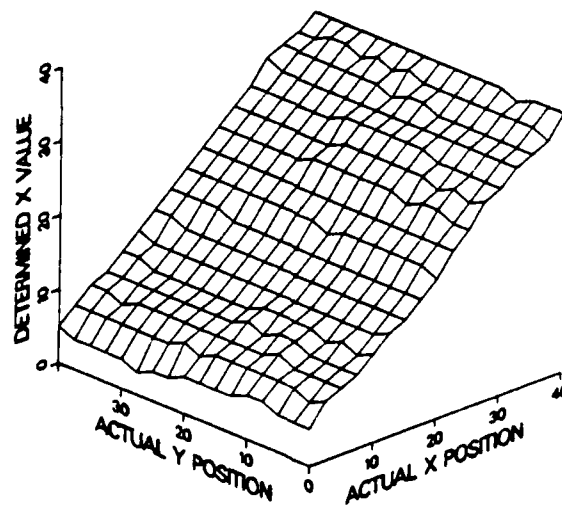


Figure 22. Uncorrected One-Dimensional Position Sensor Output Characteristics.

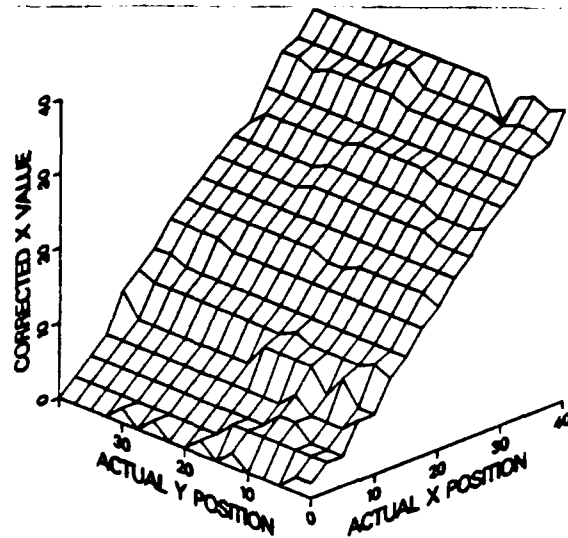


Figure 23. Corrected One-Dimensional Position Sensor Output Characteristics.

available zero-level and amplification control, the linear raw output from the one-dimensional transducer can be spread out over the available range of determined values. Elimination of the need for software data correction will increase the speed of the position measurement while decreasing the cost and complexity of the entire system.

### 3. SUMMARY

A proof-of-principle integrated hardware-software system has been developed which rapidly measures impact locations on a planar surface. The transducer for this position sensor consists of an electrically resistive square sheet with charge collection tabs along the outer edges. When electrical charge is deposited at the point of impact, the rate of charge transfer to each collection tab depends on the resistance and, therefore, the physical distance between the point of charge deposition and the tab. The impact position is deduced from the rate at which charge is transferred to the collection tabs. Two transducer geometries have been investigated. Predominantly, a four-tab arrangement has been tested which allows a single transducer to simultaneously determine position along two axes. In addition, a cursory

investigation has considered a transducer geometry with two charge collection tabs, which allows position to be measured along a single axis.

The electronic hardware which is used to process the collected charge has been tested and is documented in Appendix A. To increase the accuracy of position measurements, a collection of software routines which are used to digitize the output signal, precalibrate the system, and correct the raw position measurements has been developed. These software routines are described and listed in Appendix B. Application of the software correction utilities is shown to reduce accuracy errors by a factor of four. Relevant accuracy and precision parameters are tabulated below for errors along a single axis. Accuracy errors are also tabulated for combined two axis measurements. This data was obtained using the four-tab transducer geometry in a laboratory environment. In Table 4, "full area" indicates that the entire active surface of the position sensor was utilized while "reduced area" refers to tests in which only the central 76% of the sensor's active area was tested. Accuracy error refers to the difference between the actual position and the mean position of a large number of individual measurements. Precision error is a measure of the range of values over which the ensemble of individual measurements is spread. For these tests, the precision error was quantified by considering the range of values which contained 90% of the individual measurements. All error values are given as a percentage of the active surface edge length.

For the combined two-dimensional position measurements, the notions of accuracy and precision error were combined into a single gauge of total error. Empirical laboratory tests determined the confidence levels that 90% of all individual position measurements would fall within a circle of a given radius or position error. Simulated field testing of the position sensor yielded total errors which were equal to or smaller than those predicted by laboratory evaluation. The apparent equivalence between the performance of the position sensor in laboratory and field environments is due in part to the insensitivity of the system to the actual amount of deposited charge. This was demonstrated by varying the capacity of the charge storage capacitor over six orders of magnitude with no variation in system performance. The ability to predict field performance through laboratory testing is a particularly convenient capability.

**Table 4. Position Sensor Error Parameters**

	<b>1-Axis Maximum Accuracy Error (%)</b>	<b>1-Axis Average Accuracy Error (%)</b>	<b>1-Axis Maximum Precision Error (%)</b>	<b>1-Axis Average Precision Error (%)</b>	<b>2-Axis Maximum Accuracy Error (%)</b>	<b>2-Axis Average Accuracy Error (%)</b>
<b>Uncorrect Full Area</b>	23	6.3	—	—	30	10
<b>Uncorrect Reduced Area</b>	17	5.0	—	—	20	8.0
<b>Correct Full Area</b>	13	1.4	30	4.4	18	2.3
<b>Correct Reduced Area</b>	5.0	0.9	20	3.6	9.0	1.6

Laboratory evaluation was also utilized in a study of the system's ability to perform after sustaining transducer damage. A hole was cut into the active surface, and the error parameters were remeasured. The system displayed a minimal reduction in performance which indicates that for moderate damage, the impact position sensor will display considerable multihit capabilities.

The preliminary investigation of a one-dimensional, two-charge collection tab geometry revealed a conveniently linear transducer response. With improved signal processing, this system may obviate the need for complicated data correction. In order to obtain two-dimensional position information, two of these one-dimensional transducers would be required. The addition of a second transducer surface offers the potential for additional projectile velocity measurements.

It is stressed that the impact position sensor described in this report is a proof-of-principle device and, therefore, does not exemplify the ultimate performance which might be achieved by a refined device. In fact, it is clear that the performance of this position detector can be improved in a number of ways. Modeling of the charge transfer process on the active surface may suggest optimizing configurations for the resistive sheet and collection tabs to improve

the systems accuracy. Refinements in the signal processing electronics may reduce the error associated with measurement reproducibility. The time required to make the position measurement can be reduced in a number of ways. Analog and digital signal response times can both be halved by utilizing high-speed electronic components. And, finally, the time required for the data correction process can be reduced by employing correction look-up tables which are stored in hardwired programmable read only memory (PROM) chips rather than software-controlled computer look-up tables.

INTENTIONALLY LEFT BLANK.

#### **4. REFERENCES**

**Burr-Brown Corporation. "Instrumentation Amplifiers Sift Signals from Noise." The Handbook of Linear IC Applications, pp. 128-131, Tucson, AZ, 1987.**

**Jung, W. G. "IC Op-Amp Cookbook." Second edition, Howard W. Sams & Co., Inc., Indianapolis, IN, 1980.**

**De Jong, M. L. "Apple II Assembly Language." Howard W. Sams & Co., Inc., Indianapolis, IN, 1982.**

**INTENTIONALLY LEFT BLANK.**



**APPENDIX A:**  
**SIGNAL PROCESSING CIRCUITRY**

**INTENTIONALLY LEFT BLANK.**

**A.1 Charge Amplifier.** A schematic for the dual-channel charge amplifiers is shown in Figure A-1. Charge from opposing tabs on the position-sensing surface is feed into  $IN_1$  and  $IN_2$  to the inverting inputs of the operational amplifier. Since the noninverting inputs are tied to ground, the op amp outputs will try to maintain the inverting inputs at ground potential by feeding charge of the opposite sense through the selected feedback capacitor to the inverting input. As charge passes through the feedback capacitor, a potential develops across the capacitor of magnitude,

$$\Delta V = \Delta Q / C , \quad (A-1)$$

where  $V$  is the potential developed across capacitance  $C$  for an amount of deposited charge  $Q$ . From this equation, it can be seen that the magnitude of the output voltage can be scaled by the magnitude of the feedback capacitor. Thus, the amplification of these charge amplifiers is controlled by selection of a suitable feedback capacitor.

A large value resistor is included in parallel across the feedback capacitors to prevent the effective integration of the op amp's input bias current which, although small, would eventually saturate the amplifier. The use of a feedback resistor causes the output of the amplifier to "droop" with time. However, for the values of capacitors and resistors shown, the hold-time of the charge amplifier is sufficiently long to allow the output to be captured by the subsequent sample and hold circuitry. In addition, the relative zero levels of the two channels can be adjusted by the potentiometer connected to the op amp balance pins.

**A.2 Sample and Hold Circuitry.** A schematic of the sample and hold is shown in Figure A-2. The output signals from the charge amplifiers are fed into this circuit as *SIGNAL 1* and *SIGNAL 2*. These input signals are processed by the circuitry of IC3 to yield a voltage which is the sum of the two input signals. This summation voltage is compared against a preset threshold voltage at IC4. When the summation voltage exceeds the threshold voltage, the one-shot of IC5 is triggered. This trigger pulse serves a number of purposes and is therefore buffered using transistor T1. One task of the trigger signal is to illuminate a light emitting diode which notifies the operator that an event has occurred. The trigger signal also pulls down an active-low nonmaskable interrupt (NMI) line which can be used to synchronize associated computer-controlled data acquisition equipment. The computer used for this task

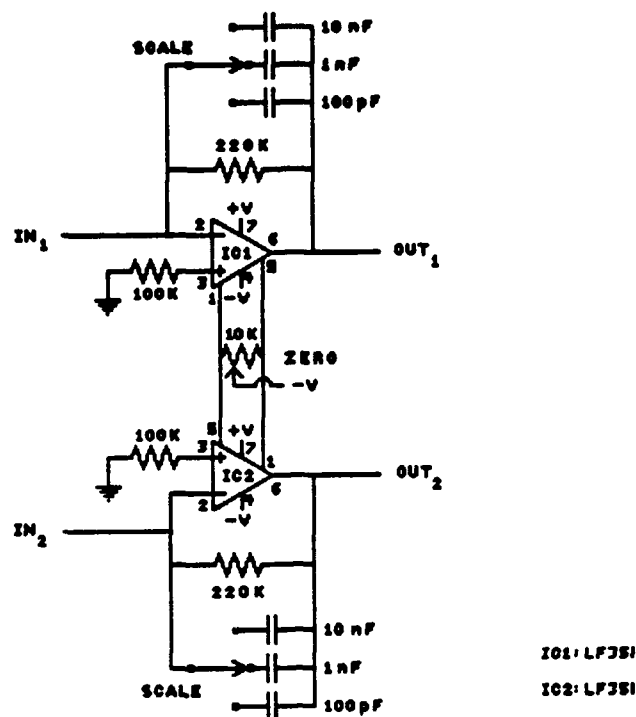


**Figure A-1. Schematic of Dual Channel Charge Amplifiers.**

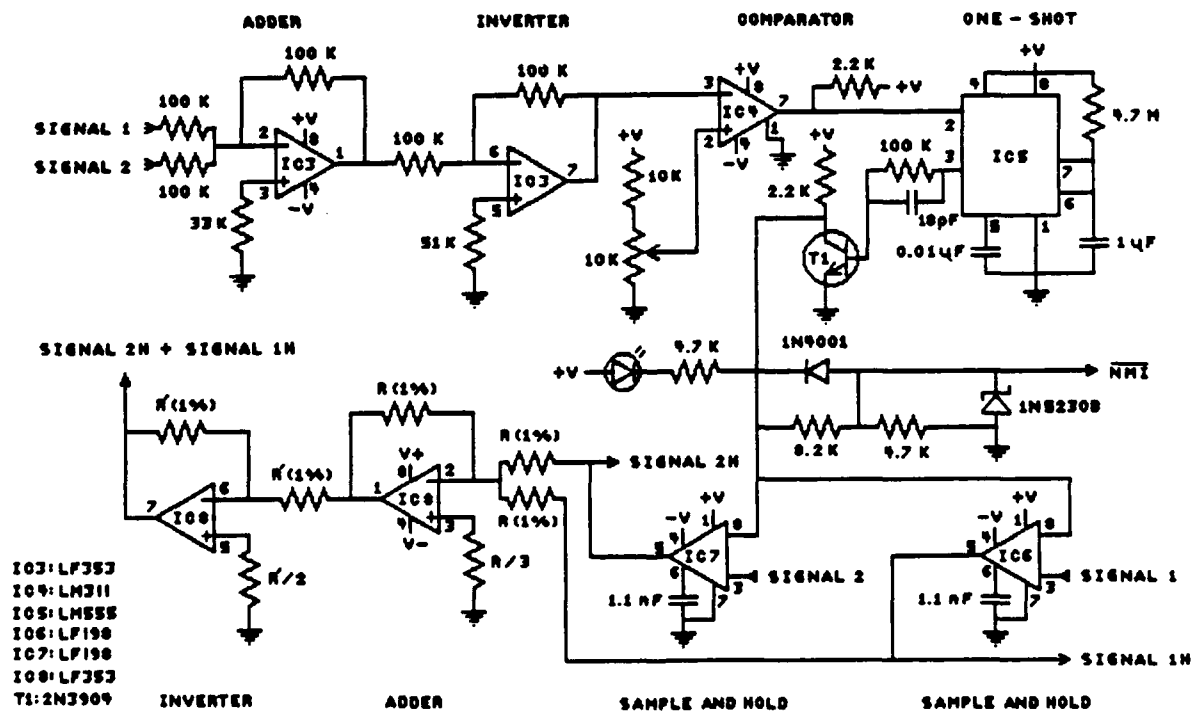


**Figure A-2. Schematic of Sample and Hold Circuitry.**

operates with 0-V to 5-V TTL signal levels. However, this sample and hold circuitry operates with +V and -V voltages of +12 and -12 V. Therefore, the trigger pulse is passed through a voltage divider for use as an NMI signal. Finally, the trigger pulse is also fed to IC6 and IC7 which sample and hold the signals from the charge amplifiers. The captured signal from *SIGNAL 2* is output as *SIGNAL 2H*. In addition, *SIGNAL 2H* is added to the captured signal *SIGNAL 1H* by IC8 and output as *SIGNAL 2H+SIGNAL 1H*.

**A.3 Analog Division Circuit.** The division of *SIGNAL 2H* by *SIGNAL 2H+SIGNAL 1H* is performed by taking the logarithms of these voltages, subtracting the logarithms, and then determining the antilogarithm of the subtraction. Such an approach is made possible by the convenient fact that for a silicon transistor, the magnitude of the base-emitter voltage,  $V_{be}$ , is a logarithmic function of the collector current,  $I_c$ , through the transistor. The circuitry which performs these tasks is shown schematically in Figure A-3 (Jung 1980).

This circuit operates as follows. Since the noninverting inputs of op amps IC9 and IC10 are tied to ground, the associated inverting inputs are maintained at an effective ground potential. Therefore, *SIGNAL 2H* sets up a current flow through its input resistor which is equal to  $(\text{SIGNAL } 2H)/R$ . This input current is equal to the collector current through transistor  $T_2$ . By the logarithmic relationship between  $I_c$  and  $V_{be}$ , it follows that the voltage drop between the base and emitter of  $T_2$  must have a magnitude which is proportional to  $\ln[(\text{SIGNAL } 2H)/R]$ . Because  $T_2$  is an npn transistor and the base is tied to ground, it follows that the sense of the voltage at the emitter of this transistor will be negative with respect to ground. By similar reasoning, the current through transistor  $T_3$  is  $(\text{SIGNAL } 2H+\text{SIGNAL } 1H)/R$  which generates a voltage between the base and emitter of  $\ln[(\text{SIGNAL } 2H+\text{SIGNAL } 1H)/R]$ . The emitter of  $T_3$  is tied to the emitter of  $T_2$  which implies that the magnitude of the potential at the emitter of  $T_3$  must be  $\ln(\text{SIGNAL } 2H/R)$ . Since  $T_3$  is an npn transistor, the conditions that the emitter is at a potential of magnitude  $\ln(\text{SIGNAL } 2H/R)$ , and the voltage drop between the base and emitter has a magnitude of  $\ln[(\text{SIGNAL } 2H+\text{SIGNAL } 1H)/R]$  requires that the base be at a potential of  $\ln(\text{SIGNAL } 2H/R) - \ln[(\text{SIGNAL } 2H+\text{SIGNAL } 1H)/R]$ . This base potential is provided by output pin 7 of IC9 and represents the difference between the logarithms of the two input signals. If the antilogarithm of this signal were taken, the required division would be completed. However, for convenience this signal is combined with another adjustable signal, referred to as *SCALE*, which is on the order of 10 V and can be used to vary the scale of the output

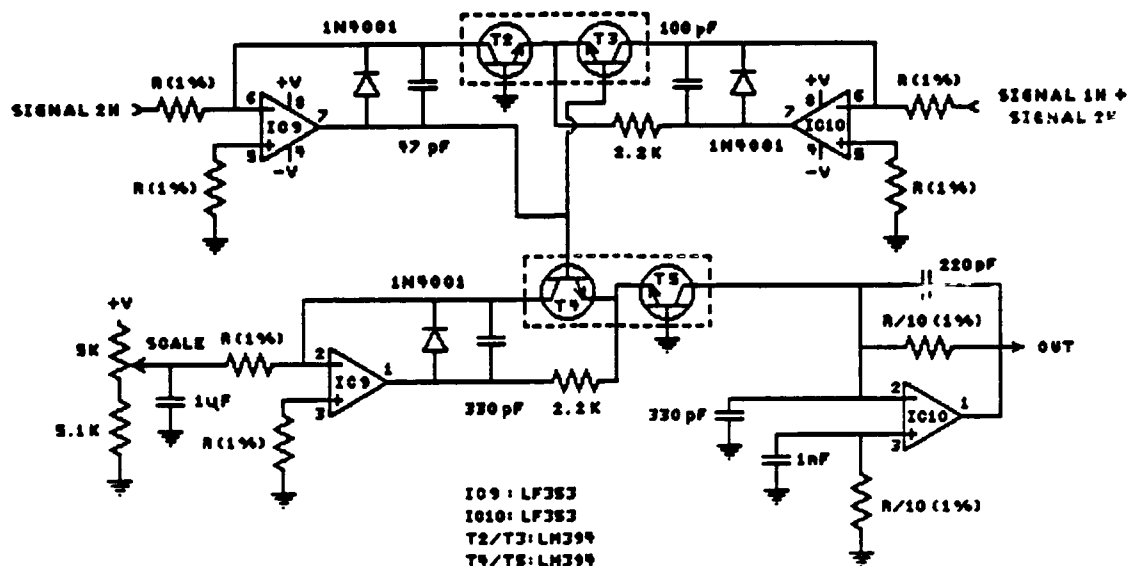


Figure A-3. Schematic of Analog Division Circuitry.

signal. Transistor  $T_4$  is configured much like  $T_3$ . Since the collector current through  $T_4$  is  $SCALE/R$ , and the base potential is set at  $\ln(SIGNAL\ 2H/R) - \ln[(SIGNAL\ 2H+SIGNAL\ 1H)/R]$ , it follows that the emitter must be at a potential of magnitude  $\ln(SCALE/R) + \ln(SIGNAL\ 2H/R) - \ln[(SIGNAL\ 2H+SIGNAL\ 1H)/R]$ . Using the laws of logarithms and the fact that all the  $R$ s are equal, this can be rewritten as:

$$\ln \left( SCALE * \frac{SIGNAL\ 2H}{SIGNAL\ 2H+SIGNAL\ 1H} \right).$$

Thus, all that is left to be done is to take the antilogarithm of the above expression, and the necessary division will have been performed, complete with a variable scaling factor. This task is accomplished by transistor  $T_5$ . Because the base of this transistor is grounded, the base to emitter voltage drop will have a magnitude equal to the above expression. A  $V_{be}$  of this magnitude allows a collector current of magnitude equal to the antilogarithm of  $V_{be}$  which is  $SCALE * SIGNAL\ 2H/(SIGNAL\ 2H+SIGNAL\ 1H)$ . This current passes through the feedback resistor of the associated op amp which has a value which is only one-tenth that of the input resistors. Therefore, the output signal is reduced by a factor of ten, which offsets the approximate factor of ten introduced by the  $SCALE$  signal, and the analog division is complete.

The various feedback capacitors are included for stability against oscillation while the clamp diodes protect the transistors against reverse biasing. For maximum temperature stability, the transistor pairs should be either monolithic transistor pairs, such as LM394's or well-matched discretes.

**A.4 Voltage Amplifier.** A differential input voltage amplifier is included as the last step of analog signal processing. The ability to vary both the DC offset and the signal amplitude allows the final output signal to be tailored for further digital signal processing or display. Through the use of differential amplifiers, common-mode noises, such as a 60-Hz "hum" and capacitively coupled microprocessor clocking signals, are greatly reduced. A schematic for the voltage amplifier is shown in Figure A-4.

Operational amplifiers IC11 and IC12 serve as very high impedance input buffers to avoid common-mode-rejection-ratio (CMRR) degradation resulting from impedance mismatch between the differential inputs. Since the inputs to these buffers are DC coupled, the input bias depends on the signal source. Therefore, high value resistors are connected from each input to ground to provide DC return paths to the amplifier's common reference (Burr-Brown Corporation 1987).

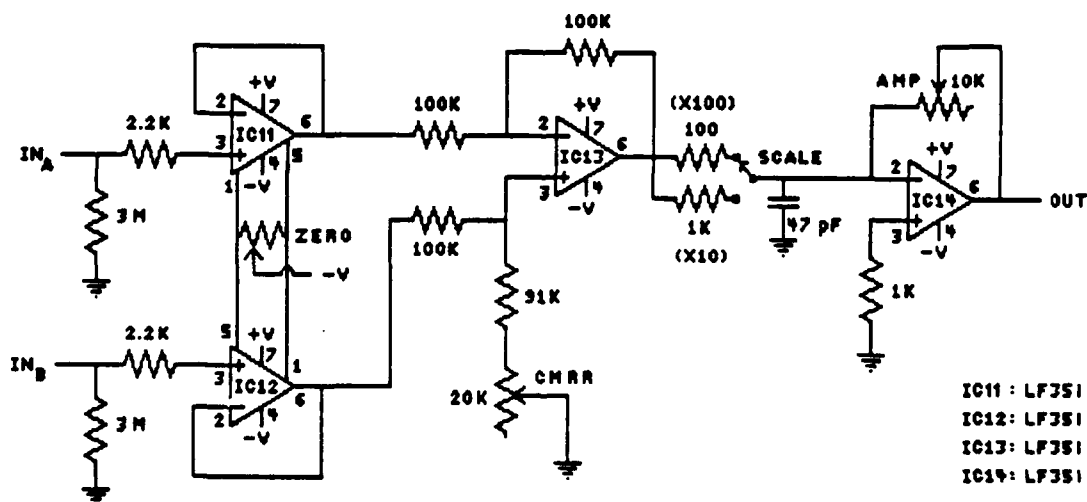


Figure A-4. Schematic of Differential Voltage Amplifier.

INTENTIONALLY LEFT BLANK.



**APPENDIX B:**  
**POSITION DETECTOR SYSTEM SOFTWARE**

INTENTIONALLY LEFT BLANK.

**B.1 Interpolation Routine.** The following Applesoft routine is designed to interpolate position sensor calibration data to a full 40 by 40 array of points. Experimental data for system calibration is not measured at all 1600 positions of a 40 by 40 grid to avoid the tedium that such a process would involve. However, in order to achieve maximum resolution for the corrected position value it is necessary to know the raw data values for a 40 by 40 grid of points.

```

100 D$ = CHR$ (4)
110 DIM XD(20,20),YD(20,20)
120 DIM XP(20),YP(20),XE(40,40),YE(40,40)
130 DIM XC(20,40),YC(20,40)
140 TEXT : HOME
150 VTAB 8
160 PRINT "THIS PROGRAM IS DESIGNED TO READ IN"
170 PRINT
180 PRINT "THE RAW DATA FROM AN EXISTING FILE"
190 PRINT
200 PRINT "AND INTERPOLATE THESE DATA VALUES TO A"
210 PRINT
220 PRINT "GRID OF DIMENSION 40 X 40"
230 PRINT : PRINT : PRINT
240 PRINT "SEE KOTTKE IF YOU HAVE ANY QUESTIONS."
250 VTAB 24
260 INPUT "ENTER A RETURN TO CONTINUE: ";A$
270 HOME
280 VTAB 12
290 PRINT "ENTER THE NAME OF THE EXISTING "
300 PRINT "CALIBRATION DATA FILE:"
310 PRINT
320 INPUT F1$
330 HOME
340 VTAB 12
350 PRINT "ENTER THE NAME OF THE INTERPOLATED"
360 PRINT "FILE TO BE CREATED:"
370 PRINT
380 INPUT F2$
390 REM *****
400 REM INPUTTING CALIBRATION DATA
410 REM *****
420 HOME
430 PRINT "INPUTTING CALIBRATION DATA"
440 PRINT
450 PRINT D$;"OPEN ";F1$
460 PRINT D$;"READ ";F1$
470 INPUT N

```

```

480 INPUT M
490 FOR I = 1 TO N
500 FOR J = 1 TO N
510 INPUT XD(I,J)
520 INPUT YD(I,J)
530 PRINT XD(I,J),YD(I,J)
540 NEXT J
550 PRINT
560 NEXT I
570 PRINT D$;"CLOSE ";F1$
580 REM *****
590 REM CALCULATING ACTUAL POSITIONS
600 REM *****
610 HOME
620 VTAB 12
630 PRINT "CALCULATING RAW DATA POSITIONS"
640 FOR I = 1 TO N
650  $XP(I) = (I - 1) * 39 / (N - 1)$ 
660  $YP(I) = (I - 1) * 39 / (N - 1)$ 
670 NEXT I
680 HOME
690 REM *****
700 REM INTERPOLATING CALIBRATION
710 REM DATA TO ALL POSSIBLE
720 REM POSITIONS.
730 REM *****
740 PRINT "INTERPOLATING CALIBRATION DATA:
750 FOR I = 0 TO 39
760 FOR J = 0 TO 39
770 IF (I < 20) THEN A = 1:B = 16:C = 1
780 IF (I > 19) THEN A = 16:B = 1:C = - 1
790 FOR K = A TO B STEP C
800 FOR L = 1 TO 16
810  $TD = ABS(I - XP(K)) + ABS(I - XP(K + 1)) +$ 
       $ABS(J - YP(L)) + ABS(J - YP(L + 1))$ 
820 IF  $(TD < = 2 * 39 / (N - 1) + 0.00001)$  THEN
      HX = K:HY = L: GOTO 860
830 NEXT L
840 NEXT K
850 PRINT "LOGIC ERROR ": STOP
860  $D1 = SQR((I - XP(HX))^2 + (J - YP(HY))^2)$ 
870  $D2 = SQR((I - XP(HX + 1))^2 + (J - YP(HY))^2)$ 
880  $D3 = SQR((I - XP(HX + 1))^2 + (J - YP(HY + 1))^2)$ 
890  $D4 = SQR((I - XP(HX))^2 + (J - YP(HY + 1))^2)$ 
900 IF (D1 = 0) THEN D1 = 0.01
910 IF (D2 = 0) THEN D2 = 0.01
920 IF (D3 = 0) THEN D3 = 0.01
930 IF (D4 = 0) THEN D4 = 0.01
940  $DT = 1 / D1 + 1 / D2 + 1 / D3 + 1 / D4$ 

```

```

950 XE(I,J) = (1 / D1) * XD(HX,HY) / DT + (1 / D2) *
      XD(HX + 1,HY) / DT + (1 / D3) * XD(HX + 1,HY + 1) /
      DT + (1 / D4) * XD(HX,HY + 1) / DT
960 YE(I,J) = (1 / D1) * YD(HX,HY) / DT + (1 / D2) *
      YD(HX + 1,HY) / DT + (1 / D3) * YD(HX + 1,HY + 1) /
      DT + (1 / D4) * YD(HX,HY + 1) / DT
970 PRINT "X=";I;" Y=";J;" XE=";INT (XE(I,J) * 100) / 100;
      "YE="; INT (YE(I,J) * 100) / 100;" HX=";HX;" HY=";HY
980 NEXT J
990 NEXT I
1000 PRINT : PRINT : PRINT
1010 PRINT "DATA READY TO BE DUMPED TO DISK": PRINT
1020 INPUT "ENTER A RETURN TO CONTINUE: ";A$
1030 PRINT D$;"OPEN ";F2$
1040 PRINT D$;"DELETE ";F2$
1050 PRINT D$;"OPEN ";F2$
1060 PRINT D$;"WRITE ";F2$
1070 FOR I = 0 TO 39
1080 FOR J = 0 TO 39
1090 PRINT XE(I,J)
1100 PRINT YE(I,J)
1110 NEXT J
1120 NEXT I
1130 PRINT D$;"CLOSE ";F2$

```

**B.2 Generate Calibration Look-Up Table Routine.** The following Applesoft routine is designed to generate a calibration look-up table for use by subsequent data correction routines. This calibration is performed by a point-by-point comparison of all possible data pairs and the previously obtained raw calibration data.

```

100 D$ = CHR$ (4)
110 DIM XA(10),YA(10)
120 DIM XE(40,40),YE(40,40)
130 DIM XC(40,40),YC(40,40)
140 TEXT : HOME
150 VTAB 8
160 PRINT "THIS PROGRAM IS DESIGNED TO GENERATE"
170 PRINT
180 PRINT "A POSITION DETECTOR LOOK UP TABLE BY"
190 PRINT
200 PRINT "DETERMINING THE CLOSEST FIT BETWEEN"
210 PRINT
220 PRINT "ALL POSSIBLE DATA VALUES AND THE"
230 PRINT

```

```

240 PRINT "INTERPOLATED CALIBRATION DATA"
250 PRINT : PRINT : PRINT
260 PRINT "SEE KOTTKE IF YOU HAVE ANY QUESTIONS."
270 VTAB 24
280 INPUT "ENTER A RETURN TO CONTINUE: ";A$
290 HOME
300 VTAB 12
310 PRINT "ENTER THE NAME OF THE EXISTING "
320 PRINT "INTERPOLATED DATA FILE."
330 PRINT
340 INPUT F1$
350 HOME
360 VTAB 12
370 PRINT "ENTER THE NAME OF THE LOOK UP TEXT"
380 PRINT "FILE TO BE CREATED:"
390 PRINT
400 INPUT F2$
410 REM *****
420 REM INPUTTING CALIBRATION DATA
430 REM *****
440 HOME
450 PRINT "INPUTTING INTERPOLATED DATA"
460 PRINT
470 PRINT D$;"OPEN ";F1$
480 PRINT D$;"READ ";F1$
490 FOR I = 0 TO 39
500 FOR J = 0 TO 39
510 INPUT XE(I,J)
520 INPUT YE(I,J)
530 PRINT XE(I,J),YE(I,J)
540 NEXT J
550 PRINT
560 NEXT I
570 PRINT D$;"CLOSE ";F1$
580 REM *****
590 REM DETERMINE BEST FIT POINT BY
600 REM POINT.
610 REM *****
620 FOR I = 0 TO 39
630 FOR J = 0 TO 39
640 LV = 10000000
650 FOR K = 0 TO 39
660 FOR L = 0 TO 39
670 TV = ABS (I - XE(K,L)) + ABS (J - YE(K,L))
680 IF (TV < LV) THEN LV = TV:NA = 1:XA(NA) = K:YA(NA) = L
690 IF (TV = LV) THEN NA = NA + 1:XA(NA) = K:YA(NA) = L
700 NEXT L
710 NEXT K
720 XC(I,J) = 0:YC(I,J) = 0

```

```

730 FOR LA = 1 TO NA
740 XC(I,J) = XC(I,J) + XA(LA)
750 YC(I,J) = YC(I,J) + YA(LA)
760 NEXT LA
770 XC(I,J) = XC(I,J) / NA
780 YC(I,J) = YC(I,J) / NA
790 IF (XC(I,J) - INT (XC(I,J)) < .5) THEN
      XC(I,J) = INT (XC(I,J))
800 IF (XC(I,J) - INT (XC(I,J)) > = .5) THEN
      XC(I,J) = INT (XC(I,J)) + 1
810 IF (YC(I,J) - INT (YC(I,J)) < .5) THEN
      YC(I,J) = INT (YC(I,J))
820 IF (YC(I,J) - INT (YC(I,J)) > = .5) THEN
      YC(I,J) = INT (YC(I,J)) + 1
830 PRINT "X=";I;" Y=";J;" XC=";XC(I,J);" YC=";YC(I,J)
840 NEXT J
850 NEXT I
860 PRINT : PRINT : PRINT
870 PRINT "READY TO DUMP LOOK UP DATA."
880 PRINT
890 INPUT "ENTER A RETURN TO CONTINUE: ";A$
900 PRINT D$;"OPEN ";F2$
910 PRINT D$;"DELETE ";F2$
920 PRINT D$;"OPEN ";F2$
930 PRINT D$;"WRITE ";F2$
940 FOR I = 0 TO 39
950 FOR J = 0 TO 39
960 PRINT XC(I,J)
970 PRINT YC(I,J)
980 NEXT J
990 NEXT I
1000 PRINT D$;"CLOSE ";F2$

```

**B.3 Data Acquisition, Correction, and Display Routine.** The following Applesoft routine is designed to load calibration data from a specified file into particular address locations, acquire A/D converter raw data, determine the corrected position, and graphically display the result. The actual acquisition of data from the A/D chip is performed by a call to a machine language driver routine which is the next listing in this appendix.

When this program is first run, the data from the specified calibration look-up data file is read in and deposited at particular computer memory locations. Specifically, the corrected X position,  $X_c$ , for the raw data pair  $(X_r, Y_r)$  is located on the memory page which is displaced by

$X_r$  pages from the base page 30h at the  $Y_r$ th memory position on that page (h indicates a hexadecimal number). The corresponding corrected Y position,  $Y_c$ , is located on the same memory page at the  $Y_r+80h$  memory position. This somewhat obscure placement of the calibration data in memory allows the indirect indexed addressing mode of the 6502 microprocessor chip to be utilized for convenient and rapid access to the corrected data (De Jong 1982). In this addressing mode, a number in a convenient zero-page location (IAL) is added to the number in the Y register to determine the low-order byte of the address of the operand (ADL). The high-order byte of the operand address (ADH) is determined by the sum of the sequential zero-page location (IAL+1) and any carry from the ADL summation (C). Symbolically, the indirect indexed addressing mode can be represented as:

$$ADL = [IAL] + [Y] \quad (B-1)$$

$$ADH = [IAL + 1] + C \quad (B-2)$$

$$operand = [ADH:ADL] , \quad (B-3)$$

where square brackets denote the contents of a memory location or address and the colon denotes concatenation. So, to determine the corrected X value,  $X_c$ , from a pair of raw data values ( $X_r, Y_r$ ), the contents of IAL are preset to 0h,  $Y_r$  is transferred to the Y register, and the contents of IAL+1 is set to  $X_r+30h$ . A simple load accumulator call (LDA) using the indirect indexed addressing mode then returns with  $X_c$  in the accumulator. Corrected values for Y are obtained in a similar manner if the contents of IAL are preset to 80h.

```

100 LOMEM: 6 * 4096
110 D$ = CHR$ (4)
120 DIM X(20,40),Y(20,40)
130 TEXT : HOME
140 VTAB 10
150 PRINT "THIS PROGRAM IS DESIGNED TO ACQUIRE"
160 PRINT
170 PRINT "DATA FROM THE GRID, LOOK UP THE "
180 PRINT
190 PRINT "CORRECTED POSITION VALUE AND "
200 PRINT
210 PRINT "GRAPHICALLY DISPLAY THE RESULTS."
220 PRINT : PRINT : PRINT

```



```

230 PRINT "SEE KOTTKE IF YOU HAVE ANY QUESTIONS."
240 VTAB 24
250 INPUT "ENTER A RETURN TO CONTINUE: ";A$
260 HOME
270 VTAB 12
280 PRINT "ENTER THE NAME OF THE TEXT FILE"
290 PRINT
300 PRINT "THAT CONTAINS THE LOOK UP TABLE"
310 PRINT
320 INPUT "DATA: ";F1$
330 PRINT D$;"OPEN ";F1$
340 PRINT D$;"READ ";F1$
350 FOR I = 0 TO 19
360 PRINT I
370 FOR J = 0 TO 39
380 INPUT X(I,J)
390 INPUT Y(I,J)
400 NEXT J
410 NEXT I
420 FOR I = 0 TO 19
430 PRINT I
440 FOR J = 0 TO 39
450 POKE 3 * 4096 + I * 256 + J, X(I,J)
460 POKE 3 * 4096 + I * 256 + 8 * 16 + J, Y(I,J)
470 NEXT J
480 NEXT I
490 FOR I = 20 TO 39
500 PRINT I
510 FOR J = 0 TO 39
520 INPUT X(I - 20,J)
530 INPUT Y(I - 20,J)
540 NEXT J
550 NEXT I
560 FOR I = 20 TO 39
570 PRINT I
580 FOR J = 0 TO 39
590 POKE 3 * 4096 + I * 256 + J, X(I - 20,J)
600 POKE 3 * 4096 + I * 256 + 8 * 16 + J, Y(I - 20,J)
610 NEXT J
620 NEXT I
630 PRINT D$;"CLOSE ";F1$
640 HOME
650 VTAB 12
660 PRINT "LOADING MACHINE CODE ROUTINE."
670 PRINT D$;"BLOAD DETECTOR MACH NOPL0T,A$2000"
680 TEXT : HOME
690 VTAB 12
700 PRINT "    DETECTOR IS ARMED"
710 REM POKING S&H DELAY AND JUMP VECTOR

```

```

720 POKE 250,2
730 POKE 10,76
740 POKE 11,0
750 POKE 12,2 * 16
760 A = USR (0)
770 XRAW = INT ( PEEK (255) * 39 / 255)
780 YRAW = INT ( PEEK (254) * 39 / 255)
790 XC = PEEK (3 * 4096 + XRAW * 256 + YRAW)
800 YC = PEEK (3 * 4096 + XRAW * 256 + 8 * 16 + YRAW)
810 HLIN 0,39 AT YC
820 VLIN 0,39 AT XC
830 VTAB 22
840 PRINT "RAW X = ";XRAW;" CORRECTED X = ";XC
850 PRINT "RAW Y = ";YRAW;" CORRECTED Y = ";YC;"
860 FOR T = 1 TO 1500: NEXT T
870 HOME
880 GOTO 680

```

B.4 Machine Language A/D Driver. This 6502 machine language routine is used to acquire data from the A/D converter chip when signalled by an active low on the nonmaskable interrupt line (NMI). The acquired data is stored in zero-page memory locations which can be accessed the controlling high level routine.

```

1          ORG $2000          ;RUN ADDR
2 *
3          JSR $FF4A          ;SAVE REG
4 *
5          LDA #$4C           ;LOAD NMI
6          STA $03FB          ;JUMP
7          LDA #<NMI          ;COMMAND
8          STA $03FC          ;AND
9          LDA #>NMI          ;ADDRESS
10         STA $03FD
11 *
12         LDA #$FF           ;SET DONE
13         STA $FB            ;FLAG
14 *
15 LOOP    LDA #$FF           ;COUNTER
16         JSR $FCA8          ;WAIT
17         STA $C030          ;SPEAKER
18         LDY $FB            ;GET FLAG
19         BNE LOOP           ;DONE ??
20         JMP STOP           ;TO EXIT
21 *

```

22 NMI	LDA #<PUNT	;NON NMI
23	STA \$03FC	;INTERUPT
24	LDA #>PUNT	;ROUTINE
25	STA \$03FD	;ADDRESS
26 *		
27	LDX \$FA	;SAMPLE
28 DELAY	DEX	;AND HOLD
29	BNE DELAY	;DELAY
30 *		
31	LDA #\$00	;SET ADC
32	STA \$C0C4	;CHANNEL
33 *		
34	LDA \$C0C1	;START CON
35 *		
36	NOP	;DELAY
37	NOP	;TO ALLOW
38	NOP	;THE EOC
39	NOP	
40	NOP	;D7 LINE
41	NOP	;TO DROP
42	NOP	
43 TESTX	LDA \$C0C2	;CONVERSN
44	BPL TESTX	;DONE ??
45 *		
46	LDA \$C0C3	;GET DATA
47 *		
48	STA \$FF	;STORE X
49 *		
50	LDA #\$01	;SET ADC
51	STA \$C0C4	;CHANNEL
52 *		
53	LDA \$C0C1	;START CON
54 *		
55	NOP	;DELAY
56	NOP	;TO ALLOW
57	NOP	;THE EOC
58	NOP	;D7 LINE
59	NOP	
60	NOP	;TO DROP
61	NOP	
62 *		
63 TESTY	LDA \$C0C2	;CONVERSN
64	BPL TESTY	;DONE ??
65 *		
66	LDA \$C0C3	;GET DATA
67 *		
68	STA \$FE	;STORE Y
69 *		
70	LDA #\$00	;DONE

71	STA \$FB	;FLAG
72 *		
73	RTI	;END NMI
74 *		
75 STOP	JSR \$F836	;CL SCR N
76 *		
77	LDA #\$0F	;SET
78	JSR \$F864	;COLOR
79 *		
80	STA \$C054	;PRI PAGE
81	STA \$C056	;LOW RES
82	STA \$C053	;TXT & GR
83	STA \$C050	;GO GRAPH
84 *		
85	JSR \$FF3F	;REP REG
86 *		
87	RTS	;GO BASIC
88 *		
89 PUNT	RTI	;NON NMI

**No. of  
Copies Organization**

- 2 Administrator  
Defense Technical Info Center  
ATTN: DTIC-DDA  
Cameron Station  
Alexandria, VA 22304-6145
- 1 Commander  
U.S. Army Materiel Command  
ATTN: AMCAM  
5001 Eisenhower Avenue  
Alexandria, VA 22333-0001
- 1 Commander  
U.S. Army Laboratory Command  
ATTN: AMSLC-DL  
2800 Powder Mill Road  
Adelphi, MD 20783-1145
- 2 Commander  
U.S. Army Armament Research,  
Development, and Engineering Center  
ATTN: SMCAR-IMI-I  
Picatinny Arsenal, NJ 07806-5000
- 2 Commander  
U.S. Army Armament Research,  
Development, and Engineering Center  
ATTN: SMCAR-TDC  
Picatinny Arsenal, NJ 07806-5000
- 1 Director  
Benet Weapons Laboratory  
U.S. Army Armament Research,  
Development, and Engineering Center  
ATTN: SMCAR-CCB-TL  
Watervliet, NY 12189-4050
- (Unclass. only)1 Commander  
U.S. Army Armament, Munitions  
and Chemical Command  
ATTN: AMSMC-IMF-L  
Rock Island, IL 61299-5000
- 1 Director  
U.S. Army Aviation Research  
and Technology Activity  
ATTN: SAVRT-R (Library)  
M/S 219-3  
Ames Research Center  
Moffett Field, CA 94035-1000

**No. of  
Copies Organization**

- 1 Commander  
U.S. Army Missile Command  
ATTN: AMSMI-RD-CS-R (DOC)  
Redstone Arsenal, AL 35898-5010
- 1 Commander  
U.S. Army Tank-Automotive Command  
ATTN: ASQNC-TAC-DIT (Technical  
Information Center)  
Warren, MI 48397-5000
- 1 Director  
U.S. Army TRADOC Analysis Command  
ATTN: ATRC-WSR  
White Sands Missile Range, NM 88002-5502
- 1 Commandant  
U.S. Army Field Artillery School  
ATTN: ATSF-CSI  
Ft. Sill, OK 73503-5000
- (Class. only)1 Commandant  
U.S. Army Infantry School  
ATTN: ATSH-CD (Security Mgr.)  
Fort Benning, GA 31905-5660
- (Unclass. only)1 Commandant  
U.S. Army Infantry School  
ATTN: ATSH-CD-CSO-OR  
Fort Benning, GA 31905-5660
- 1 Air Force Armament Laboratory  
ATTN: WL/MNOI  
Eglin AFB, FL 32542-5000
- Aberdeen Proving Ground
- 2 Dir, USAMSAA  
ATTN: AMXSY-D  
AMXSY-MP, H. Cohen
- 1 Cdr, USATECOM  
ATTN: AMSTE-TC
- 3 Cdr, CRDEC, AMCCOM  
ATTN: SMCCR-RSP-A  
SMCCR-MU  
SMCCR-MSI
- 1 Dir, VLAMO  
ATTN: AMSLC-VL-D
- 10 Dir, BRL  
ATTN: SLCBR-DD-T

No. of

Copies Organization

- 5    **Commander**  
U.S. Army Tank-Automotive Command  
ATTN: AMSTA-RSS, Dr. J. Thompson  
      AMSTA-RSK, T. Furmaniak  
      ASM-SS-T,  
      J. Rowe  
      T. Dean  
      ASM-SS, COL Miller  
Warren, MI 48397-5000
- 2    **Defense Advanced Research Projects**  
      **Agency**  
ATTN: LTC Pat Sullivan  
      Tom Hafer  
3701 North Fairfax Drive  
Arlington, VA 22203-1714
- 2    **Director**  
Lawrence Livermore National Laboratory  
University of California  
ATTN: C-Group/Physics,  
      Raymond Gogolewski  
      Mark Wilkins  
P.O. Box 808  
Livermore, CA 94550
- 1    **Director**  
Los Alamos National Laboratory  
ATTN: Jim Kennedy, M-7  
Mail Stop P950  
Los Alamos, NM 87545

# USER EVALUATION SHEET/CHANGE OF ADDRESS

**This laboratory undertakes a continuing effort to improve the quality of the reports it publishes. Your comments/answers below will aid us in our efforts.**

1. Does this report satisfy a need? (Comment on purpose, related project, or other area of interest for which the report will be used.) \_\_\_\_\_

2. How, specifically, is the report being used? (Information source, design data, procedure, source of ideas, etc.)

- 3. Has the information in this report led to any quantitative savings as far as man-hours or dollars saved, operating costs avoided, or efficiencies achieved, etc? If so, please elaborate.**

4. General Comments. What do you think should be changed to improve future reports? (Indicate changes to organization, technical content, format, etc.) \_\_\_\_\_

BRL Report Number BRL-TR-3302 Division Symbol

Check here if desire to be removed from distribution list. \_\_\_\_\_

Check here for address change. \_\_\_\_\_

**Current address:**      **Organization** \_\_\_\_\_  
                                  **Address** \_\_\_\_\_

**DEPARTMENT OF THE ARMY**  
Director  
U.S. Army Ballistic Research Laboratory  
ATTN: SLCBR-DD-T  
Aberdeen Proving Ground, MD 21005-5066

**OFFICIAL BUSINESS**

**BUSINESS REPLY MAIL**

**FIRST CLASS PERMIT No 0001, APG, MD**

**Postage will be paid by addressee.**

**Director  
U.S. Army Ballistic Research Laboratory  
ATTN: SLCBR-DD-T  
Aberdeen Proving Ground, MD 21005-5066**

NO POSTAGE  
NECESSARY  
IF MAILED  
IN THE  
UNITED STATES